



Enhancement of output power density and performance of direct borohydride-hydrogen peroxide fuel cell using Ni-Pd core-shell nanoparticles on polymeric composite supports (rGO-PANI) as novel electrocatalysts



Raana Mahmoodi^a, Mir Ghasem Hosseini^{a,b,*}, Haleh Rasouli^a

^a Department of Physical Chemistry, Electrochemistry Research Laboratory, University of Tabriz, Tabriz, Iran

^b Engineering Faculty, Department of Materials Science and Nanotechnology, Near East University, 99138, Nicosia, North Cyprus, Mersin 10, Turkey

ARTICLE INFO

Keywords:

C_{Ni}-S_{Pd} nanoparticles
Single borohydride fuel cell
Reduced graphene oxide
Polyaniline
Polymeric composites

ABSTRACT

In this research work, Ni-Pd nanoparticles with core-shell structure (C_{Ni}-S_{Pd}) were synthesized on different catalyst supports such as reduced graphene oxide (rGO), pure polyaniline (PANI) and polymeric composites of rGO with PANI (rGO-PANI) for the first time. In polymeric composite supports, the ratio of rGO to PANI was altered (0.36, 0.14 and 0.11). That way, after chemical reduction of graphene oxide to rGO with sodium borohydride, different polymeric composite supports of rGO-PANI were prepared by chemical oxidation of different amounts of aniline monomer with ammonium persulfate (APS) in rGO dispersions and named as rGO-PANI1 (rGP1), rGO-PANI2 (rGP2) and rGO-PANI3 (rGP3). X-ray diffraction (XRD), field emission scanning electron microscopy (FE-SEM), energy-dispersive X-ray spectroscopy (EDX), transmission electron microscopy (TEM), high-resolution transmission electron microscopy (HR-TEM), fourier transform infrared (FT-IR) spectra, inductively coupled plasma mass spectrometry (ICP-MS) analysis and X-ray photoelectron spectrometer (XPS) were employed to study the morphology and crystal structure of the novel nanostructures. Catalytic behavior of the catalysts respect to NaBH₄ oxidation was evaluated in half-cell configuration and in direct borohydride-hydrogen peroxide fuel cell. The cyclic voltammetry results showed that C_{Ni}-S_{Pd}/rGP1 has the highest borohydride oxidation current density (42678 A. g⁻¹) respect to C_{Ni}-S_{Pd}/PANI (17072 A. g⁻¹), C_{Ni}-S_{Pd}/rGO (39085 A. g⁻¹), C_{Ni}-S_{Pd}/rGP2 (32260 A. g⁻¹) and C_{Ni}-S_{Pd}/rGP3 (24954 A. g⁻¹). As well as, the single fuel cell studies indicated that with C_{Ni}-S_{Pd}/rGP1 as anodic electrocatalyst, power density (339.10 mW.cm⁻²) was enhanced as 64.54% and 8.52% in comparison with C_{Ni}-S_{Pd}/PANI (120.23 mW.cm⁻²) and C_{Ni}-S_{Pd}/rGO (310.20 mW.cm⁻²), respectively. These consequences imply that the rGP1 polymeric composite with the ratio of rGO/PANI = 0.36 is a suitable support substance that can improves the electroactivity for borohydride oxidation considerably.

1. Introduction

The confined fossil fuel resources along with environmental problems have led researchers to seek renewable energy resources such as supercapacitors [1], batteries [2], solar cells [3] and fuel cells [4]. Recently, fuel cell technology has attracted more attention due to high power density, high efficiency and low to zero emissions. Fuel cells considered as feasible energy converters because convert the chemical energy of fuel and oxidant directly into electrical energy [5,6]. Among various kinds of fuel cells, proton exchange membrane fuel cells (PEMFCs) are favorable power technology for many application in transportable, mobile power sources and automotive engines [7].

Among PEM fuel cells, direct borohydride fuel cells (DBFCs) with acidic H₂O₂ as oxidant and alkaline sodium borohydride present several benefits as high theoretical potential, faster reaction kinetics, ease of transportation and its storage [8–11]. The main issue for PEMFCs commercialization is the synthesis of low price catalysts that has excellent catalytic activity and stability under the experimental environment. Due to both of these reasons, PEM fuel cell catalysts have been considered to be the great participants on its performance. Electrocatalysts where the electrochemical reactions happen consist of a support that is chemically inert with deposited nanoparticles (NPs) of metals that are catalytically active. Support should be able to transport electrons and ions produced during electrochemical reactions on the

* Corresponding author at: Department of Physical Chemistry, Electrochemistry Research Laboratory, University of Tabriz, Tabriz, Iran.
E-mail address: mg-hosseini@tabrizu.ac.ir (M.G. Hosseini).

surface of the catalyst particles so it has to have good ionic and electronic conductivity, high porosity and surface area. Different metallic NPs with alloy structure that composed of noble metal and transition metal were synthesized and studied for borohydride oxidation reaction (BOR). These NPs showed higher electroactivity than simple noble metal electrocatalysts because of the synergistic effect between the two metals [12–20]. Compared with alloy structure, core-shell NPs with noble metal as shell and transition metal as core are assumed possible applicants as anodic catalysts due to their individual and new characteristics [21,22]. As catalytic reactions happen on the surface of the NPs, a large content of metal in the core of the NPs is wasted. As a result, a noble metal at outer surface and base metal second atomic layer instead of noble metal as electrocatalyst are of major importance for the use level improvement of noble metal. On the other hands, core-shell structure decreases the noble metal loading and increases their utilization. Recently, different core-shell NPs were synthesized and used as electrocatalysts in *direct borohydride fuel cell* applications for example Duan et. al. achieved a maximum power density of 74 mW.cm^{-2} at 20°C using $\text{C}_{\text{Ni}}\text{-S}_{\text{Au}}/\text{C}$ as anodic electrocatalyst [23]. Also, this group obtained the maximum power density as high as 39.8 mW.cm^{-2} at 20°C using $\text{C}_{\text{Cu}}\text{-S}_{\text{Pd}}/\text{C}$ as anodic electrocatalyst [24]. In another work, with $\text{C}_{\text{Cu}}\text{-S}_{\text{Ag}}/\text{C}$ as anodic electrocatalyst, direct borohydride-hydrogen peroxide fuel cell (DBHPFC) exhibits a maximum anodic power density of 17.27 mW.mg^{-1} [25]. Also, Duan et. al obtained the maximum anodic power density as high as 8.54 mW.cm^{-2} at 25°C using $\text{C}_{\text{Ni}}\text{-S}_{\text{Ag}}/\text{C}$ as anodic electrocatalyst and Pt mesh (1 cm^2) as cathodic electrode [26]. Wang et. al. reached to power density of 68.21 mW.cm^{-2} using $\text{C}_{\text{Au}}\text{-S}_{\text{Pd}}/\text{C}$ as anodic catalyst and Au/C as cathodic catalyst [27]. Among the nonprecious metals, nickel has received much attention because of specific characteristics like great durability in alkaline environments and great performance for borohydride adsorption and having the negative E° [28]. Also, noble metals such as Ru, Pt and Pd have excellent catalytic activity in various reactions but exist at very low levels of abundance [29,30]. The recent literatures showed that Pd-based electrocatalysts instead of Pt and Ru [31,32] have excellent electroactivity toward BOR in alkaline media compared with Pt and Ru and as well as palladium is slightly inexpensive than platinum. Therefore in this study, N I-P d core-shell NPs ($\text{C}_{\text{Ni}}\text{-S}_{\text{Pd}}$) were selected and used for BOR and fuel cell studies.

As mentioned previously, catalyst support has also critical role on the catalyst performance. On the other words, support has significance effect on the size, degree of dispersion, distribution and stabilization of catalyst particles [33]. Different carbon materials have been used as catalyst supports for *oxygen reduction reaction* $\text{C}_{\text{Co}}\text{-S}_{\text{Pt}}/\text{C}$ [34], $\text{C}_{\text{Ni}}\text{-S}_{\text{Pt}}/\text{C}$ [35] and *methanol oxidation* $\text{C}_{\text{Co}}\text{-S}_{\text{Pt}}/\text{MWCNT}$ [36], $\text{C}_{\text{Ru}}\text{-S}_{\text{Pt}}/\text{C}$ [37], $\text{C}_{\text{Ni}}\text{-S}_{\text{Pt}}/\text{C}$ [35]. Instead of traditional carbon supports (Vulcan and MWCNTs) for the electrocatalysts, nanosized carbon supports can be used effectively to reduce NPs loading. Graphene has attracted significant regard recently [38] because of the its high electrical and thermal conductivities [39], great mechanical strength [40], large specific surface area, and low manufacturing cost [41]. These make the graphene suitable for different applications such as electronic and energy storage devices [42], and nanocomposites [43]. Different methods such as mechanical exfoliation, epitaxial growth and chemical vapor deposition have been used for graphene synthesis that chemically synthesized graphene using graphite is a useful component in different composites [44]. Many studies were done using core-shell NPs on graphene support for *oxygen reduction reaction* $\text{C}_{\text{PdPt}}\text{-S}_{\text{Pt}}/\text{rGO}$ [45], $\text{C}_{\text{Pt}}\text{-S}_{\text{Au}}/\text{rGO}$ [46], $\text{C}_{\text{AuPd}}\text{-S}_{\text{Pd}}/\text{rGO}$ [47] and for *methanol oxidation* $\text{C}_{\text{Co}}\text{-S}_{\text{Pt}}/\text{rGO}$ [48], $\text{C}_{\text{Pb}}\text{-S}_{\text{Pt}}/\text{rGO}$ [49], $\text{C}_{\text{AuPd}}\text{-S}_{\text{Pd}}/\text{rGO}$ [47].

Specifically, the composites of graphene and polymers have attracted more considerations due to their special properties arising from the high conductivity and reinforcement of graphene nanofillers [50]. Conducting polymers also have been widely investigated and extensively used in different organic devices [51,52]. Among different conducting polymers, PANI is an identical candidate for applied

applications due to its good process ability, environmental stability, low cost and reversible control of electrical properties by both charge transfer doping and protonation [53].

The composites of PANI with reduced graphene oxide allow a facile flow of electronic charges through the polymer matrix in electrochemical reactions. PANI acts additional tasks in electrochemical reactions because causes a low ohmic drop to the bulk and limits mass transfer for the electroactive species to reach the catalytic sites. As well as, metallic particles could be spread into the matrix of these polymers. Using an appropriate combination of PANI and rGO, novel electrocatalysts could be produced with higher surface areas and increased catalytic activities toward the oxidation of fuels [54,55]. On the other hands, embedding of rGO in conducting polymeric matrices such as PANI for various nanocomposite materials is now a popular area.

Based on our awareness and literature review as mentioned before, there are no studies present about the use of $\text{C}_{\text{Ni}}\text{-S}_{\text{Pd}}$ core-shell NPs on rGO, PANI and on rGO-PANI composites for *borohydride oxidation* and in *single borohydride-hydrogen peroxide fuel cell* applications.

Herein, based on above considerations, for the first time, we synthesized $\text{C}_{\text{Ni}}\text{-S}_{\text{Pd}}/\text{PANI}$, $\text{C}_{\text{Ni}}\text{-S}_{\text{Pd}}/\text{rGO}$ and $\text{C}_{\text{Ni}}\text{-S}_{\text{Pd}}/\text{rGP}$ electrocatalysts. The catalytic behavior of the catalysts respect to BOR were investigated with three electrode set-up using cyclic voltammetry (CV), chronamperometry (CA), chronopotentiometry (CP), electrochemical impedance spectroscopy (EIS) techniques. Also, the influence of rGO/PANI ratio in polymeric composite supports on the catalytic activity of polymeric electrocatalysts was evaluated. As well as, the effect of different electrocatalysts ($\text{C}_{\text{Ni}}\text{-S}_{\text{Pd}}/\text{rGO}$, $\text{C}_{\text{Ni}}\text{-S}_{\text{Pd}}/\text{PANI}$ and $\text{C}_{\text{Ni}}\text{-S}_{\text{Pd}}/\text{rGP}$) on the efficiency of single DBHPFC were evaluated. In addition to, the current-voltage and current-power density curves in fuel cell, the behavior of the cell EIS was investigated. The results of DBHPFC and cell EIS were applied for choice the great anodic catalyst.

2. Experimental

2.1. Synthesis of $\text{C}_{\text{Ni}}\text{-S}_{\text{Pd}}/\text{rGO}$ electrocatalyst

At first graphene oxide (GO) was produced from natural graphite (Sinchem, SK 4206.0500, Cas.No: 7782-42-5, Made in South Korea) by Hummer's method [56]. The synthesized GO was characterized using Perkin-Elmer FT-IR spectrophotometer. $\text{C}_{\text{Ni}}\text{-S}_{\text{Pd}}$ NPs were then prepared on rGO via continuous reduction technique. Briefly, the produced graphene oxide (128 mg) was spread in water ultrasonically. Next, NiCl_2 (0.04 g) and tri-sodium citrate (0.06 g) solutions were drop by drop poured, respectively and spread for another hour. Next, alkaline solution of NaBH_4 as reducing agent was added droply and refluxed for three hours at 100°C . The obtained sample was filtered, washed and dried at 70°C . Then, Ni/rGO was spread in ethylene glycol (EG) for two hours. Adequate contents of PdCl_2 dissolved in HCl were added it. Using NaOH/EG solution, the pH was increased to 7–8. After stirring the mixture for 4 h at 95°C , $\text{C}_{\text{Ni}}\text{-S}_{\text{Pd}}/\text{rGO}$ were gathered, washed and dried at 80°C .

2.2. Synthesis of $\text{C}_{\text{Ni}}\text{-S}_{\text{Pd}}/\text{PANI}$ electrocatalyst

Initially, PANI was synthesized by *in situ* chemical oxidative polymerization of aniline monomer (Fluka, AG chem. Fabrik, CH-9470 Buchs, distilled prior to use) with ammonium persulfate (APS, Merck) as the oxidant in 1 M HCl solution. Aniline (0.5 M) was dissolved in 100 ml of 1 M HCl. Then an aqueous solution of APS in 1 M HCl was added to initiate the polymerization of aniline and the reaction continued in an ice bath. After 6 h, the resulting suspension product was filtered and washed with distilled water until the filtrate become colorless. The collected sample dried at 40°C in vacuum oven for 24 h. $\text{C}_{\text{Ni}}\text{-S}_{\text{Pd}}/\text{PANI}$ were produced via continuous reduction technique on pure PANI. Therefore, 80 mg PANI was spread in N-Methyl-2-pyrrolidone (NMP). Then NiCl_2 , tri-sodium citrate, NaBH_4 and NaOH according to

the Section 2.1 was added to the homogenous suspension. Ni/PANI was obtained at the end of this step. For synthesize $C_{Ni-S_{Pd}}/PANI$, EG was used as reducing agent in accordance with Section 2.1.

2.3. Synthesis of $C_{Ni-S_{Pd}}/rGP1$, $C_{Ni-S_{Pd}}/rGP2$ and $C_{Ni-S_{Pd}}/rGP3$ electrocatalysts

Before synthesis the electrocatalysts, the catalyst supports was first prepared. So, different rGO-PANI composites with various ratios of rGO to PANI (0.36, 0.14 and 0.11) in rGO-PANI composite were obtained (rGP1, rGP2 and rGP3). The typical procedure is as follows: the different amounts of aniline monomer (0.3, 0.6 and 0.9 mL) in 1 M HCl solution was added to the suspension of 80 mg rGO in the mixture of ethanol: distilled water (3:1) and was dispersed with the help of ultrasound. Then an aqueous solution of APS in 1 M HCl was added to initiate the polymerization of aniline and the reaction continued in an ice bath for 6 h. The obtained composites washed with distilled water and the resulting product was then dried under vacuum at 40 °C. The resulted composite supports were named as rGO-PANI1 (rGP1), rGO-PANI2 (rGP2) and rGO-PANI3 (rGP3). In the next step, $C_{Ni-S_{Pd}}/rGP$ electrocatalysts were synthesized according to the procedure explained in the Section 2.2 with this difference 80 mg of rGP1, rGP2 and rGP3 were used as support instead of pure PANI. The obtained electrocatalysts were named $C_{Ni-S_{Pd}}/rGP1$, $C_{Ni-S_{Pd}}/rGP2$ and $C_{Ni-S_{Pd}}/rGP3$. The loading of metals in synthesized electrocatalysts was 20 wt%. The synthesis procedure was shown in Fig. 1.

2.4. Electrochemical characterization

For three electrode studies, a platinum sheet was used as a counter electrode, the potentials were measured with respect to a mercury/mercury oxide electrode (MOE) and working electrodes were prepared by mixing 5 mg of catalyst powders with isopropyl alcohol, distilled water and Nafion 5 wt% and 6 μ L of the prepared ink containing 0.0013 mg metal was put on GC. Electrochemical experiments were done using an Origalys (Origalys-OGF01A/Potentiostat/Galvanostat, France). Electroactivity of the synthesized catalysts for BOR were evaluated by three electrode techniques in alkaline solution of $NaBH_4$.

The important section of the fuel cell is membrane electrode assembly (MEA). The catalyst inks are sprayed on both sides of Nafion membrane with the surface area of 5 cm^2 using catalyst coated membrane (CCM) technique because of the advantages of this method [57–59]. The catalyst ink was provided by dispersing of the Pt/C (0.5 mg. cm^{-2}) and different anodic electrocatalysts ($C_{Ni-S_{Pd}}/rGO$, $C_{Ni-S_{Pd}}$

$/PANI$ or $C_{Ni-S_{Pd}}/rGP1$) (1 mg. cm^{-2}) in Nafion solution, distilled water and isopropyl alcohol for two hours. The effect of anodic electrocatalysts was evaluated on current-voltage, current-power density and EIS curves. The durability experiments were carried out by stabilizing the current in 50 mA.

2.5. Catalyst characterization

Morphological studies of the synthesized electrocatalysts were performed with a field FE-SEM (MIRA3FEG-SEM, Tescan), TEM (LEO 906 E (100 kV)) and HR-TEM (FEI Tecnai F20 S/TEM electron microscope). The elemental and structural investigations of the catalysts were done using EDX (Tescan operated at applied potential of 10 kV), XRD (Philips-PW 1730) and XPS (K-alpha, Thermo scientific) with monochromatic Al K α radiation as the X-ray source. FT-IR spectra were recorded on Perkin-Elmer FT-IR spectrophotometer (500–4000 cm^{-1}). ICP-MS analysis was performed using GBC6 XL ICP mass spectrometer.

3. Results and discussion

3.1. The structural and morphological characterization of the synthesized electrocatalysts

The FE-SEM images of $C_{Ni-S_{Pd}}/rGO$, $C_{Ni-S_{Pd}}/PANI$ and $C_{Ni-S_{Pd}}/rGP1$, $C_{Ni-S_{Pd}}/rGP2$ and $C_{Ni-S_{Pd}}/rGP3$ electrocatalysts in two different scales were shown in Fig. 2(a, b), (c, d), (e, f), (g, h) and (i, j), respectively. In $C_{Ni-S_{Pd}}/rGO$ electrocatalyst, the sheet-like structure of rGO support can be seen (Fig. 2(a, b)). The electrochemically surface area of rGO was increased due to its planner structure. After depositing core-shell NPs on the reduced graphene oxide surface, NPs were distributed homogenously on the rGO layers and coated its surface entirely without evident accumulation. In $C_{Ni-S_{Pd}}/PANI$ electrocatalyst, polyaniline as catalyst support shows spherical structures and the $C_{Ni-S_{Pd}}$ NPs cover its surface uniformly (Fig. 2(c, d)). This spherical structure causes to the generation of pores in the electrocatalyst and this surface porosity supplies a higher surface area for electroactive specious. In $C_{Ni-S_{Pd}}/rGP$ polymeric composite electrocatalysts ($C_{Ni-S_{Pd}}/rGP1$, $C_{Ni-S_{Pd}}/rGP2$ and $C_{Ni-S_{Pd}}/rGP3$) which the catalyst support is a combination of polyaniline and reduced graphene oxide, we expected that both the planner structure of reduced graphene oxide and the spherical structure of polyaniline can be observed in FE-SEM images. But as it can be seen in Fig. 2(e), (g) and (i), the planner structure of reduced graphene oxide only can be observed in Fig. 2(e) and with increasing the amount of aniline monomer in the synthesis medium, PANI covered the surface of

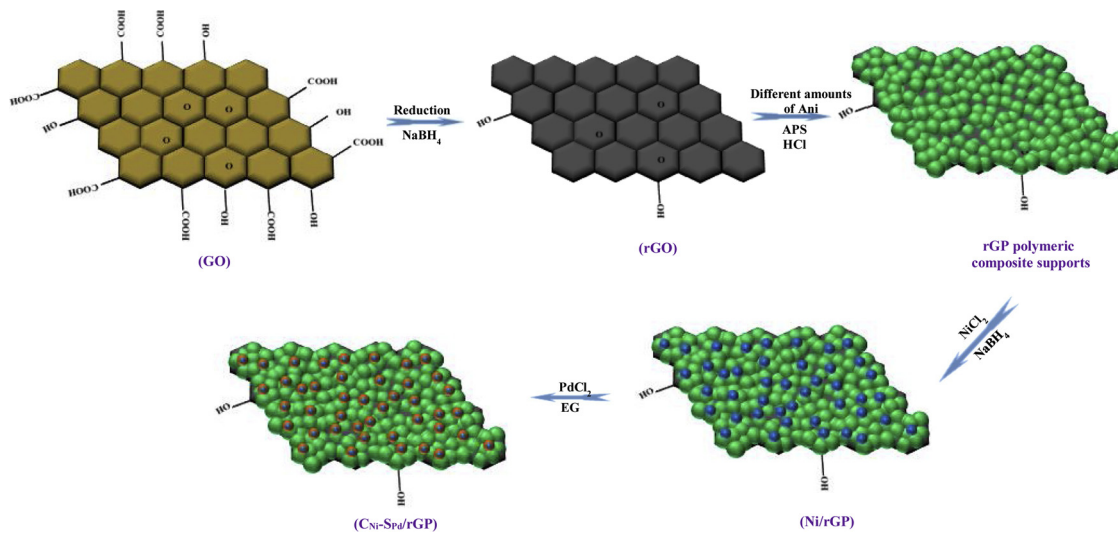


Fig. 1. The synthesis procedure of $C_{Ni-S_{Pd}}$ NPs on rGP polymeric composite supports.

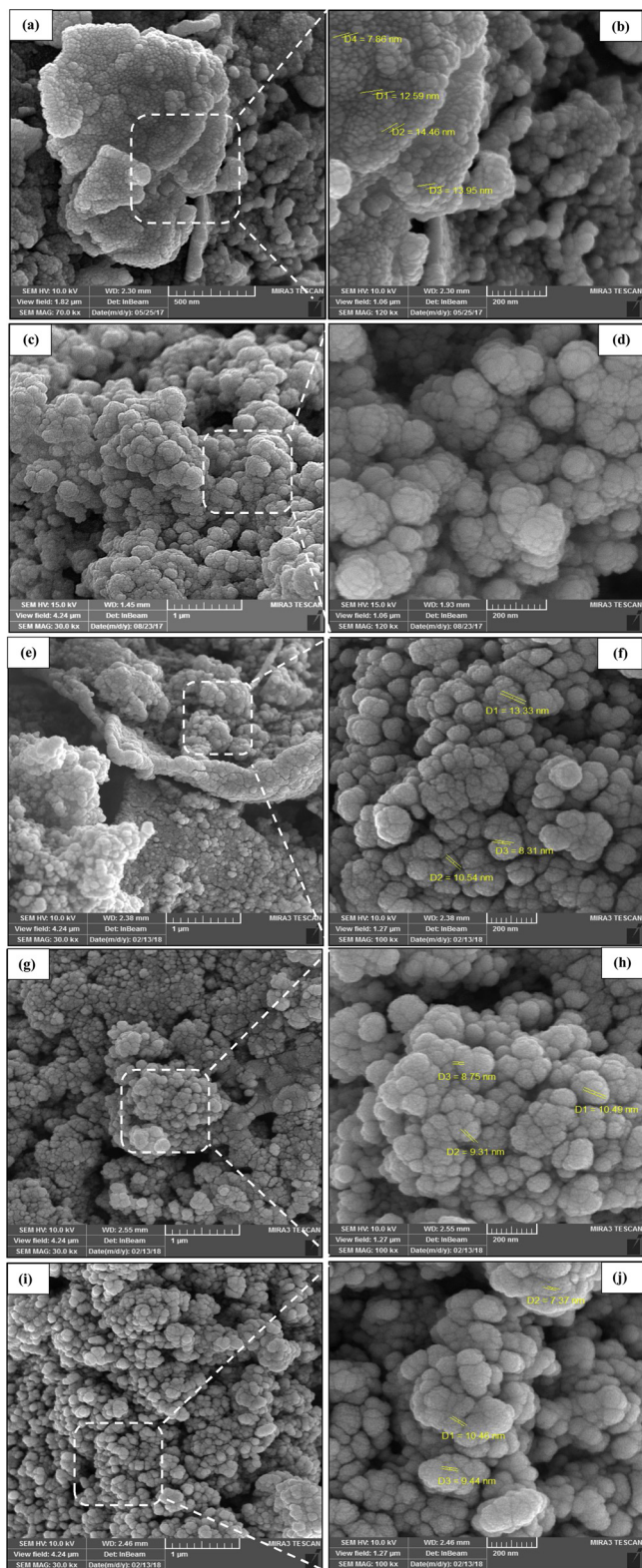


Fig. 2. The FE-SEM images of (a, b) C_{Ni-S_Pd}/rGO , (c, d) $C_{Ni-S_Pd}/PANI$ and (e, f) $C_{Ni-S_Pd}/rGP1$, (g, h) $C_{Ni-S_Pd}/rGP2$ and (i, j) $C_{Ni-S_Pd}/rGP3$ electrocatalysts.

the reduced graphene oxide and the planner structure wasn't observed instead the spherical structure of PANI can be observed. Also, the C_{Ni-S_Pd} NPs uniformly cover the surface of rGP polymeric composites (Fig. 2(f), (h) and (j)). The mean size of NPs is less than 20 nm.

The EDX spectra of C_{Ni-S_Pd}/rGO , $C_{Ni-S_Pd}/PANI$ and $C_{Ni-S_Pd}/rGP1$, $C_{Ni-S_Pd}/rGP2$ and $C_{Ni-S_Pd}/rGP3$ electrocatalysts were displayed in

Table 1

The determined metal content of C_{Ni-S_Pd} by ICP-MS analysis.

| Electrocatalyst | Pd loading wt % | Ni loading wt % |
|--------------------|-----------------|-----------------|
| C_{Ni-S_Pd}/rGO | 9.5 | 9.6 |
| $C_{Ni-S_Pd}/PANI$ | 10.1 | 9.5 |
| $C_{Ni-S_Pd}/rGP1$ | 9.8 | 9.9 |
| $C_{Ni-S_Pd}/rGP2$ | 9.9 | 9.9 |
| $C_{Ni-S_Pd}/rGP3$ | 9.7 | 9.8 |

Figures S1 (a), (b), (c), (d) and (e), respectively. Figure S1 (a) presents the peaks of C, Ni and Pd elements confirming the deposition of Ni and Pd NPs on reduced graphene oxide nanosheets. In Figures S1 (b–e), in addition to Ni, Pd and C peaks, the nitrogen peak also appears and confirms the presence of polyaniline in the catalysts structure. As well as, with increasing the amount of aniline in rGP1, rGP2 and rGP3 polymeric composite supports, the weight percentage of N was increased. The molar portion of palladium to nickel is around 1. Since EDX is a localized technique and the exact determination of metals weight percentage is difficult so the metal content of C_{Ni-S_Pd} was also checked by ICP-MS analysis (Table 1). According to Table 1, the loading of Pd and Ni on electrocatalysts is about 10 wt%.

The TEM images of rGO, rGP1 polymeric composite and $C_{Ni-S_Pd}/rGP1$ electrocatalyst were presented in Fig. 3(a), (b) and (c, d), respectively. The observed wrinkles in Fig. 3(a) confirm the laminar and transparent structure of reduced graphene oxide. In Fig. 3(b), the bright layered structure is due to the presence of rGO and the black masses confirm the existence of polyaniline in composite structure and verify that the polymerization of aniline monomer on the surface of the reduced graphene oxide sheet was done successfully. As well as, the TEM images of $C_{Ni-S_Pd}/rGP1$ composite in two different scales were shown in Fig. 3(c, d). The layered structure of the rGO sheet along with the black masses of polyaniline was clearly observed in these Figures. Also, the C_{Ni-S_Pd} NPs were dispersed on the rGO-PANI1 polymeric composite support as black particles. Due to the contrast disagreement between core and shell substances, HR-TEM was applied to support the organization of core-shell structure. Considering the fact that all electrocatalysts were synthesized using the same method (continuous reduction technique) so we only use HR-TEM image of the C_{Ni-S_Pd} on rGO support (Fig. 3e) and one of the composite supports (rGP1, Fig. 3f) to confirm the formation of core-shell structure with this method. According to Fig. 3e and f, the middle of the nanoparticles is a little bit darker than them sides. On the other hands, the contrast differences between core and shell materials were observed and illustrated the formation of core-shell structure. The mean size of NPs was approximately computed 10 nm.

To confirm the synthesis of electrocatalysts, the XRD patterns of GO, C_{Ni-S_Pd}/rGO , $C_{Ni-S_Pd}/PANI$, $C_{Ni-S_Pd}/rGP1$, $C_{Ni-S_Pd}/rGP2$ and $C_{Ni-S_Pd}/rGP3$ were depicted in Fig. 4. In the XRD pattern of GO, the strong and sharp peak at $2\theta = 11.41^\circ$ corresponds to an interlayer distance of (002) in GO. Further the reduction of GO to rGO in C_{Ni-S_Pd}/rGO reveals a broad peak at $2\theta = 24.5^\circ$ [60]. On the other hands, the removal of the sharp peak in graphene oxide associated with the appearance of a broad peak in C_{Ni-S_Pd}/rGO shows that the oxidation of graphite followed by the reduction of GO gives rGO nanosheets. In XRD pattern of $C_{Ni-S_Pd}/PANI$, the broad peak at $2\theta = 21.5^\circ$ is related to pure PANI as catalyst support and suggested PANI has amorphous structure. For three other electrocatalysts ($C_{Ni-S_Pd}/rGP1$, $C_{Ni-S_Pd}/rGP2$ and $C_{Ni-S_Pd}/rGP3$), that the catalyst support is a composite of rGO and polyaniline, the overlapping of PANI and rGO peaks causes the broad peak at $2\theta = 20-30^\circ$. In XRD patterns of C_{Ni-S_Pd}/rGO , $C_{Ni-S_Pd}/PANI$, $C_{Ni-S_Pd}/rGP1$, $C_{Ni-S_Pd}/rGP2$ and $C_{Ni-S_Pd}/rGP3$, the peaks at $2\theta = 39.15^\circ$, 45.20° , 66.20° and 79.15° are respectively associated to (111), (200), (220) and (311) facets of palladium with fcc structure [61]. The diffraction peaks of Ni weren't appeared in the XRD patterns of electrocatalysts. This can be attributed to the presence of Ni nanoparticles as amorphous phase in

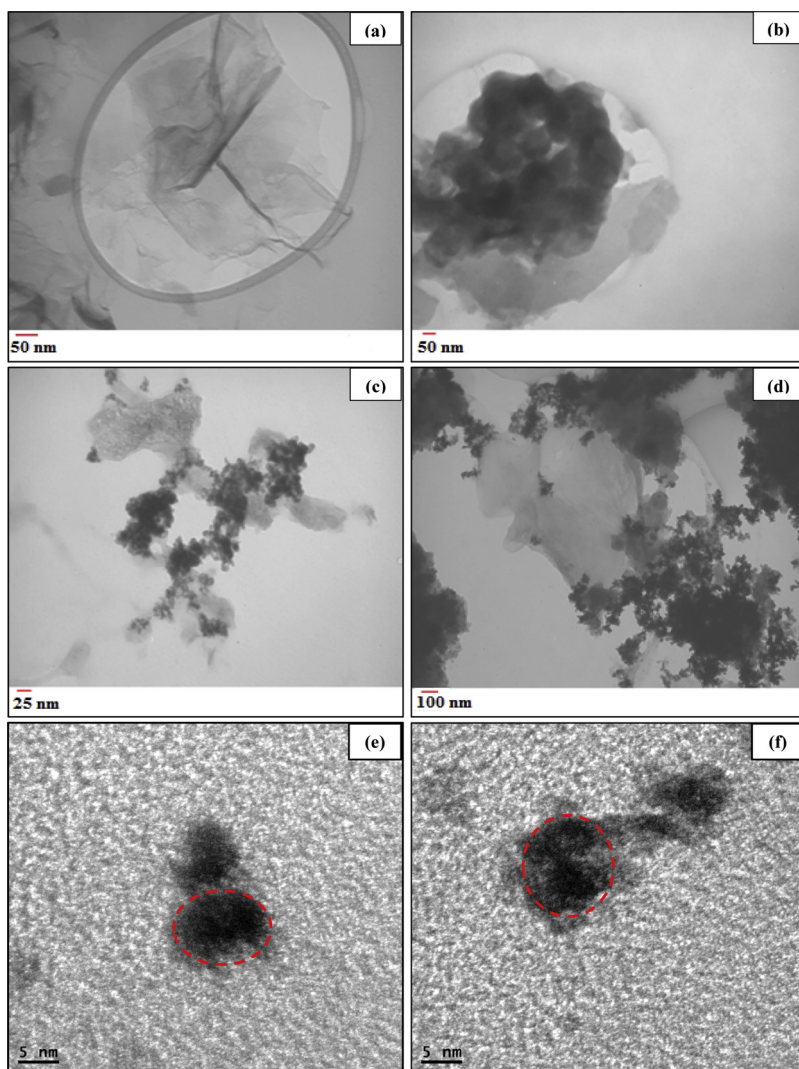


Fig. 3. TEM images of (a) rGO, (b) rGP1 polymeric composite support, (c, d) $\text{C}_{\text{Ni}}\text{-Spd}/\text{rGP1}$ electrocatalyst, HR-TEM of (e) $\text{C}_{\text{Ni}}\text{-Spd}$ on rGO and (f) on rGP1.

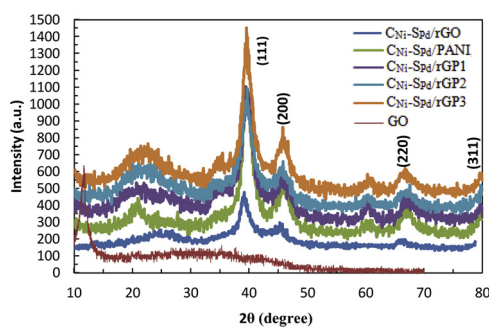


Fig. 4. The XRD spectra of GO, $\text{C}_{\text{Ni}}\text{-Spd}/\text{rGO}$, $\text{C}_{\text{Ni}}\text{-Spd}/\text{PANI}$, $\text{C}_{\text{Ni}}\text{-Spd}/\text{rGP1}$, $\text{C}_{\text{Ni}}\text{-Spd}/\text{rGP2}$ and $\text{C}_{\text{Ni}}\text{-Spd}/\text{rGP3}$.

the electrocatalysts or as very small crystalline particles that cannot be detected by XRD analysis. On the other hand, the XRD patterns of electrocatalysts exhibited two additional diffraction peaks at $2\theta = 35^\circ$ and 60° that reveals the formation of nickel oxide during the synthesis procedure [62].

The FT-IR spectra of GO and reduced GO supported $\text{C}_{\text{Ni}}\text{-Spd}$ NPs were illustrated in Fig. 5 (a). In graphene oxide spectrum, several peaks can be observed: 3360 cm^{-1} (O–H stretching vibration), 1738 cm^{-1} (C=O stretching vibrations of carbonyl/carboxyl), 1637 cm^{-1} (the vibration of carboxyl groups), 1265 cm^{-1} (C–OH stretching vibrations)

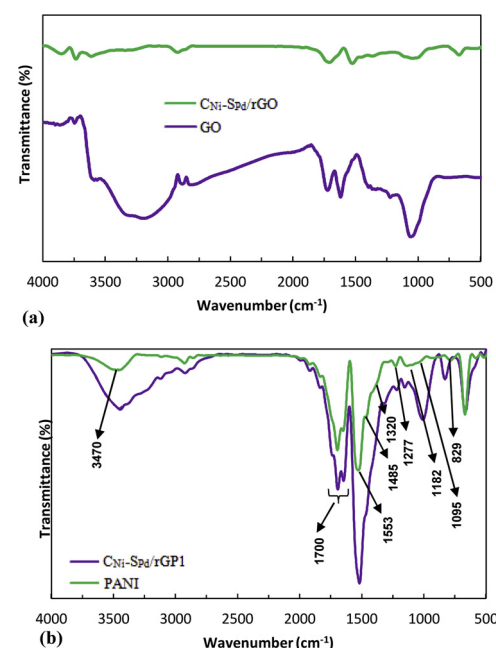


Fig. 5. FT-IR spectra of (a) GO and $\text{C}_{\text{Ni}}\text{-Spd}/\text{rGO}$, (b) PANI and $\text{C}_{\text{Ni}}\text{-Spd}/\text{rGP1}$.

and 1085 cm^{-1} (C–O stretching vibrations) [63]. With chemical reduction of GO to rGO using sodium borohydride, the intensity of oxygen functional groups on the surface of GO was decreased. The comparison of FT-IR spectra confirms that the reduction of GO to rGO has been done successfully.

To confirm the existence of polyaniline in the structure of composite electrocatalysts, the FT-IR spectrum of $\text{C}_{\text{Ni}}\text{-S}_{\text{Pd}}/\text{rGP1}$ along with the spectrum of pure polyaniline was shown in Fig. 5(b). The spectra of the other composite electrocatalysts weren't presented in Fig. 5(b), because it causes the spectrum to become tumultuous. In the FT-IR spectrum of pure polyaniline, the peak observed in the region of $3470\text{--}3200\text{ cm}^{-1}$ is related to the stretching vibrations of the N–H group in the polyaniline skeleton. The peaks at 1553 cm^{-1} and 1485 cm^{-1} regions are related to the stretching vibrations of C=N and C=C in the quinonoid and benzenoid rings of the polyaniline structure. The peaks at 1320 cm^{-1} , 1277 cm^{-1} and 1182 cm^{-1} are related to stretching vibration of C–N (aromatic amines), C–NH $_{\cdot}$ and B–NH $^{+}$ =Q, respectively. Finally, the peak relating to doping located at 1095 cm^{-1} is assigned to the C–H bending vibration in the plane, while the peak contained in 829 cm^{-1} is associated to the out of plane C–H bending vibrations for the 1,4-disubstituted aromatic ring [64–68]. The appearance of above mentioned bands indicates that PANI is in the emeraldine salt form. Also, the presence of polyaniline peaks in the $\text{C}_{\text{Ni}}\text{-S}_{\text{Pd}}/\text{rGP1}$ electrocatalyst confirms the successful synthesis of this electrocatalyst with composite support.

XPS spectra were used to clarify the surface chemical composition of the synthesized electrocatalysts. The C 1s spectra of GO and rGO in $\text{C}_{\text{Ni}}\text{-S}_{\text{Pd}}/\text{rGO}$ electrocatalyst were presented in Fig. 6(a) and (b), respectively. The C 1s spectrum of graphene oxide with peak-fitting curves in Fig. 6(a) shows six typical components: $\text{sp}^2\text{ C=C}$ (284.59 eV), $\text{sp}^3\text{ C-C}$ (285.37 eV), C–OH (287.03 eV), C–O–C (287.68 eV), C=O (289.10 eV), O–C=O (293.63 eV) [69,70]. The XPS spectrum of GO exhibited a high atomic ratio of carbon to oxygen (C/O) of 0.68. All of the six typical peaks were observed in C 1s spectrum of rGO in Fig. 6(b) with this difference that the C/O ratio increased from 0.68 to 2.54, indicating that most oxygenated groups have been removed by reduction of GO to rGO during electrocatalyst synthesis with sodium borohydride as reducing agent. Also, C 1s peaks in the rGO spectra slightly shift to lower binding energy (284.12, 284.66, 285.07, 286.31, 287.89 and 291.11 eV) respect to GO due to the electronic effect created from the existence of metal on reduced graphene oxide sheets [71]. The N 1s spectra of PANI and rGP1 composite as polymeric catalyst support were shown in Fig. 6(c) and (d), respectively. Both XPS spectra of N 1s can be deconvoluted into three peaks as shown in Fig. 6(c) and (d). In XPS spectrum of the N 1s in PANI support, the major benzenoid amine component ($-\text{NH-}$) peak is observed at 399.8 eV along with a small quinoid imine ($=\text{NH-}$) peak at 399.2 eV. The shoulder peak at a high binding energy of about 400.7 eV is ascribed to positively charged nitrogen ($-\text{NH}^{+}$), which confirms that some nitrogen (N) has been transmitted into protonated nitrogen species (N^{+}). When PANI was polymerized on reduced graphene oxide, the N^{+} peak (400.8 eV) of the rGP1 composite has a higher binding energy than pure PANI; the highest binding energy peak is due to the protonated amine units. The ratio of $[\text{N-}]/[\text{NH-}]$ provides a direct evaluation of the intrinsic oxidation state of PANI and is indicative of the polymeric level [72]. Therefore, the value of $[\text{N-}]/[\text{NH-}]$ for rGP1 composite (0.998) is obviously higher than that of pure PANI (0.614), indicating the rGP1 composite have a higher degree of doping which is due to the introduction of rGO. However, the appearance of N 1s peaks in XPS spectrum of rGP1 composite confirms that the PANI is coated on the surface of reduced graphene oxide successfully. Also, the existence of N^{+} suggests that the PANI in both support approaches a conductive emeraldine salt state and the increasing of N^{+} ratio of 2.99% to 4.27% also illustrates that nitrogen protons are successfully doped in composite support and it can improve the electrical conductivity of the composite catalyst support respect to pure PANI as catalyst support [73].

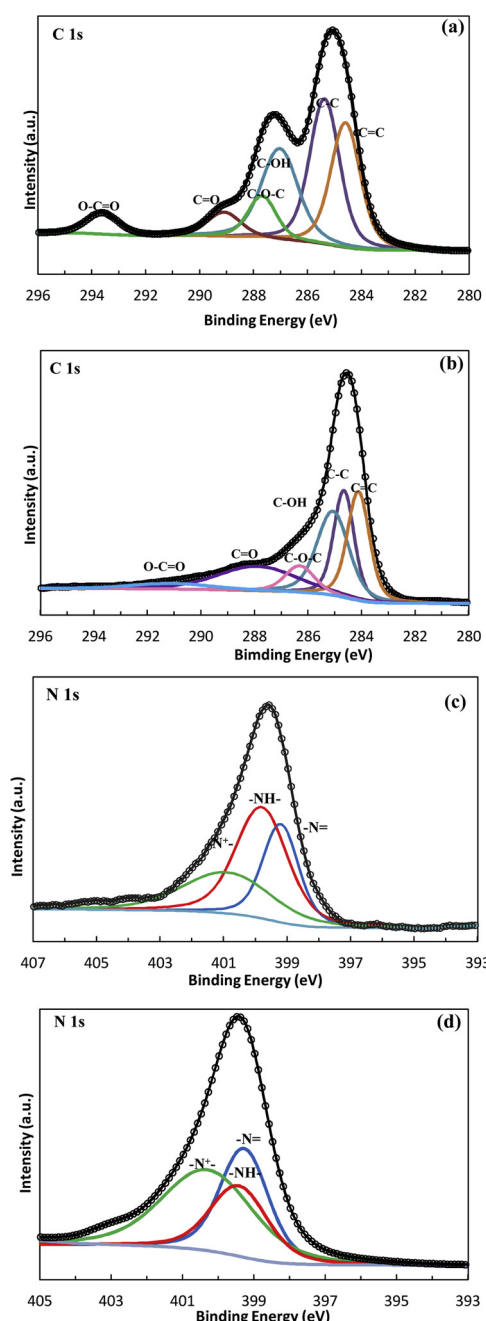


Fig. 6. The XPS spectra of C 1s in (a) GO and (b) $\text{C}_{\text{Ni}}\text{-S}_{\text{Pd}}/\text{rGO}$; N 1s in (c) PANI and (d) rGP1 composite as catalyst support.

3.2. The mechanism of electron transport

The chemical and electrochemically stable PANI not only limits the agglomeration interactions between the rGO layers, but also increases the durability of the rGO and protects it from exposure to corrosive media. Compared to rGO, which is generally incompatible with inorganic materials, PANI is electrically conductive material and can interact with other metals much more easily because it has N atoms in its structure. Therefore, the newly obtained rGO-PANI supported nanocomposite should exhibit extremely high catalytic activity and stability in direct borohydride fuel cells [74]. On the other hands, PANI can homogeneously arrange on the rGO templates as a result of the strong π – π conjugated interactions between PANI and rGO. The strong π – π interaction between the graphene structure and aromatic rings of polyaniline would facilitate electron delocalization and improve the

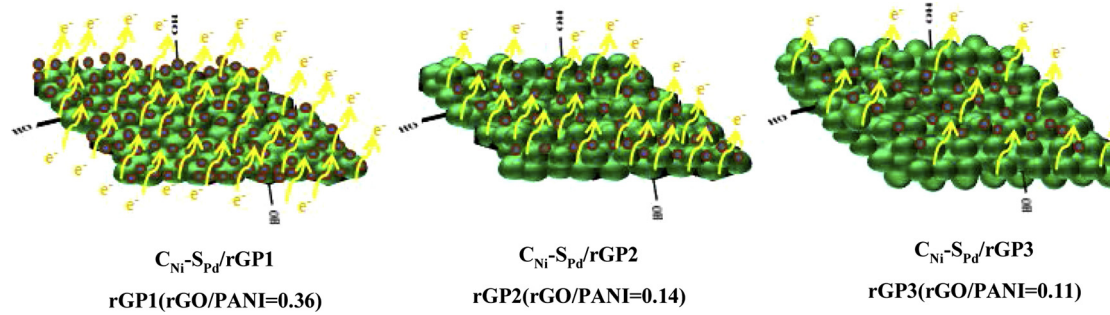
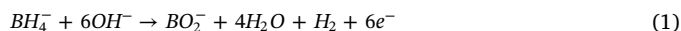


Fig. 7. The pictorial representation of electron transport mechanism.

electrical conductivity of the composites [75].

Using a pictorial representation the mechanism of electron transport was explained and correlated with the morphological structure as follow:

The ratio of rGO/PANI in rGP composite supports has important effect on the performance of catalyst electrochemically active surface area (ECSA) and its electroactivity toward BOR. It is accepted that aniline monomers could be efficiently absorbed onto the surface of rGO sheets due to the electrostatic attraction, and a kind of weak charge transfer complex formed, in which the rGO sheet acted as electron acceptor and aniline monomers as electron donor. As the support material, the rGO sheets would provide high surface area and numerous active sites for nucleation of aniline monomer, preventing the PANI nanoparticles from aggregating [76]. Furthermore, strong $\pi - \pi$ interaction between PANI chains and rGO sheet makes PANI more planar [77]. It is expected that homogeneous PANI thin layer coated on the surface of rGO sheets with large surface area and high conductivity should be favorable for increasing ECSA and dispersing catalyst nanoparticles and enhancing charge transport of the nanocomposite according to Fig. 7. It is believed that the thickness of the PANI layer played a crucial role in determining the catalytic properties of the rGO/PANI composite supports. More clearly, the larger thickness of the PANI layer formed at higher amounts of Ani monomer (0.6 mL, 0.9 mL), that is to say, larger PANI fraction, indicating more loose structure formed for a thicker layer. Therefore, the charge transfer routes and the ECSA for catalyst nanoparticles were decreased due to the loose structure. At relatively small fraction of aniline monomers, strong interaction between graphitic structures and conjugated polymeric chains causes very thin, uniform, and tightly stacked of the PANI layer on the surface of the rGO sheets. Therefore, the charge transfer was increased and borohydride oxidation reaction happens easily on the rGP1 composite support (Eq. (1)). With the further increase in the thickness of the PANI layer, the interaction force between two components became weakened, as a result, the PANI layer had a relatively loose structure. These results indicate that with the decreasing of the rGO/PANI weight ratio from 0.36 to 0.14 and 0.11, the interaction between graphene sheet and polymeric chains became weakened, which could further support the formation of more loose structure at higher PANI fraction [78]. SEM images confirmed the above explanations. In lower Ani fraction, a thin layer of PANI was formed on rGO and the layered structure of rGO can be observed (Fig. 2e). In high amounts of Ani, the thicker layer of PANI was formed on rGO with loose structure and the planer structure wasn't observed instead the spherical structure of PANI can be observed (Fig. 2 g, i).



As mentioned previously, the rGO support is good electron acceptors, while PANI can be considered as a good electron donor [79]. The rGO perform a doping agent role for PANI in the composite. The PANI may serve as “conducting bridges” among the rGO sheets. However, when the content of PANI is too high, pure PANI aggregates and the conductivity of rGO/PANI descends. As analyzed above, we confirmed

that the resultant electrical conductivity of rGO/PANI can be adjusted by the feeding ratio of rGO to aniline [80]. Therefore, the newly obtained rGO-PANI supported nanocomposite should exhibit extremely high catalytic activity and stability in DBFCs.

3.3. Electrochemical measurements

Cyclic voltammograms (CVs) of $C_{Ni-S_{Pd}}/rGO$, $C_{Ni-S_{Pd}}/PANI$, $C_{Ni-S_{Pd}}/rGP1$, $C_{Ni-S_{Pd}}/rGP2$ and $C_{Ni-S_{Pd}}/rGP3$ electrocatalysts were recorded in NaOH 1 M solution as shown in Fig. 8 (a). The peaks at the potential region of -0.65 to -0.1, 0.515 to 0.428 and 0.016 to -0.460 V are associated to hydrogen desorption peak, the transformation of $NiOOH/Ni(OH)_2$ and reduction of Pd surface oxide, respectively. These peaks were completely described in our previous works [31,59]. The ECSA was calculated from the required charge for PdO reduction which was signed with dashed circle in Fig. 8(a) [61] according to Eq. (2):

$$ECSA = \frac{Q_{PdO}}{0.405 \times [Pd]} \quad (2)$$

Q_{PdO} is the needed charge for PdO reduction (mC) and 0.405 is the charge related to surface Pd oxide stripping peak ($mC \cdot cm^{-2}$). [Pd] is Pd loading on the GC (mg). The ECSA values were calculated equal with 85, 342, 350, 180 and $145 \text{ m}^2 \cdot \text{g}^{-1}$ for $C_{Ni-S_{Pd}}/PANI$, $C_{Ni-S_{Pd}}/rGO$, $C_{Ni-S_{Pd}}/rGP1$, $C_{Ni-S_{Pd}}/rGP2$ and $C_{Ni-S_{Pd}}/rGP3$, respectively. Considering the ECSA values for all electrocatalysts and among different catalyst

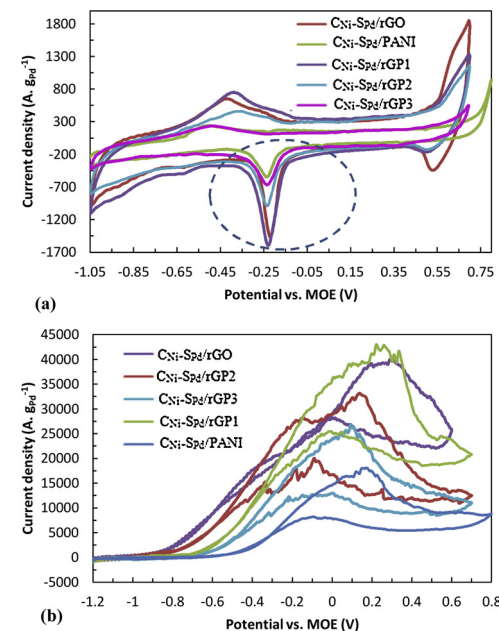


Fig. 8. CV curves of $C_{Ni-S_{Pd}}/rGO$, $C_{Ni-S_{Pd}}/PANI$, $C_{Ni-S_{Pd}}/rGP1$, $C_{Ni-S_{Pd}}/rGP2$ and $C_{Ni-S_{Pd}}/rGP3$ modified electrodes in (a) NaOH 1 M and (b) NaOH 1 M containing $NaBH_4$ 0.1 M.

supports, pure PANI exhibited the lowest electrochemical active surface area and rGO showed larger ECSA respect to pure PANI due to having the layered structure and the highest electrical conductivity respect to pure PANI. The comparison of ECSA values showed that when rGO and PANI were composite together, ECSA was increased respect to pure PANI because the conductivity of rGP composites with variant proportions is bigger than that of pure PANI produced under the similar experimental situation. Also, between rGP composites, rGP1 showed the highest ECSA. On the other hands, when the proportion of rGO/PANI is equal with 0.36, the obtained electrocatalyst shows the highest conductivity and ECSA. As described before, the rGO is specified for their large surface area suggesting narrow dispersion of $C_{Ni-S_{Pd}}$ NPs on the surface while PANI enhances the electronic passage through its conjugated chain structure. However, when the content of PANI is too high, pure PANI accumulates and the conductivity of rGP composite decreases. As described before, we established that the consequent electrical conductivity of rGP composites may be controlled by the feeding proportion of Ani to rGO. So, rGP1 composite increases the ECSA and as a result the reaction sites [81].

The CV curves of $C_{Ni-S_{Pd}}/rGO$, $C_{Ni-S_{Pd}}/PANI$, $C_{Ni-S_{Pd}}/rGP1$, $C_{Ni-S_{Pd}}/rGP2$ and $C_{Ni-S_{Pd}}/rGP3$ electrocatalysts in a solution of NaOH 1 M containing NaBH₄ 0.1 M were presented in Fig. 8(b). The peak was observed in forward scan is related to borohydride oxidation and the peak in reverse scan is associated to oxidation of BH_3OH^- produced in BOR. The current density of BO on different electrocatalysts is as follow:

$C_{Ni-S_{Pd}}/PANI$ (17072 A. g⁻¹) < $C_{Ni-S_{Pd}}/rGP3$ (24954 A. g⁻¹) < $C_{Ni-S_{Pd}}/rGP2$ (32260 A. g⁻¹) < $C_{Ni-S_{Pd}}/rGO$ (39085 A. g⁻¹) < $C_{Ni-S_{Pd}}/rGP1$ (42678 A. g⁻¹)

Borohydride oxidation current density on $C_{Ni-S_{Pd}}/rGP1$ is 4.49, 1.71, 1.32 and 1.09 times higher than that of on $C_{Ni-S_{Pd}}/PANI$, $C_{Ni-S_{Pd}}/rGP3$, $C_{Ni-S_{Pd}}/rGP2$ and $C_{Ni-S_{Pd}}/rGO$, respectively. As the current density values show when the proportion of rGO/PANI is equal with 0.36, the composite catalyst has the highest borohydride oxidized peak current density because of the results mentioned above. Therefore it can be deduced that the composite catalyst has the superior electroactivity as the proportion of rGO/PANI is 0.36. It has been also observed that when PANI is combined with rGO in the direction of the obtained results, the activity against borohydride has great efficiency. Therefore, composite supports (rGP) changed the activity and durability of the electrocatalyst. The adsorption rate of the borohydride molecule was also more enhanced by enhancing the active surface area with rGP1 polymeric composite support. On the other words, supporting the $C_{Ni-S_{Pd}}$ NPs with rGP1 hindered the electrocatalytic reduction toward BOR and observed that the catalytic activity was much higher than that of the singular $C_{Ni-S_{Pd}}/PANI$ or $C_{Ni-S_{Pd}}/rGO$.

Fig. 9 shows the effect of temperature on the CV curves in NaOH 1 M and NaBH₄ 0.1 M at a scan rate of 100 mV.s⁻¹. Increasing the temperature from 298.15 K to 328.15 K resulted in the increase of the peak current for all electrocatalysts and with increasing temperature, cathodic shift was observed for the anodic peaks (Fig. 9(a–e)). For each electrocatalyst, the plots of the peak current density against the 1/T remain linear (Fig. 9(f)) so as expected, electrocatalysts exhibit an Arrhenius-type behavior, described by Eq. (3) [82].

$$E_a = -R \cdot \partial(Lni_p) / \partial \left(\frac{1}{T} \right) \quad (3)$$

T: temperature (K), R: gas constant (kJ. mol⁻¹), i_p: peak current density (A. g⁻¹) and E_a: activation energy (kJ. mol⁻¹). By applying the Arrhenius equation, E_a for $C_{Ni-S_{Pd}}/PANI$, $C_{Ni-S_{Pd}}/rGO$, $C_{Ni-S_{Pd}}/rGP1$, $C_{Ni-S_{Pd}}/rGP2$ and $C_{Ni-S_{Pd}}/rGP3$ electrocatalysts was calculated and found to be 30.59, 16.77, 16.59, 17.94 and 20.37 kJ.mol⁻¹, respectively. As expected, among the synthesized electrocatalysts, $C_{Ni-S_{Pd}}/rGP1$ has the lowest activation energy and so shows the highest catalytic activity for BOR.

The electroactivity of the catalysts for BOR was evaluated using

chronoamperometry in NaOH 1 M + NaBH₄ 0.1 M solution by polarizing at -0.2 V for $C_{Ni-S_{Pd}}/PANI$, $C_{Ni-S_{Pd}}/rGO$, $C_{Ni-S_{Pd}}/rGP1$, $C_{Ni-S_{Pd}}/rGP2$ and $C_{Ni-S_{Pd}}/rGP3$ electrocatalysts and the corresponding curves were shown in Fig. 10(a). All of the electrocatalysts showed current decay during BH₄⁻ electrooxidation. After about 100 s, the $C_{Ni-S_{Pd}}/rGP1$ showed the highest steady state current density (22300 A. g⁻¹) followed by the $C_{Ni-S_{Pd}}/rGO$ (20800 A. g⁻¹), $C_{Ni-S_{Pd}}/rGP2$ (16600 A. g⁻¹), $C_{Ni-S_{Pd}}/rGP3$ (9700 A. g⁻¹) and $C_{Ni-S_{Pd}}/PANI$ (2900 A. g⁻¹) electrodes. The $C_{Ni-S_{Pd}}/rGP1$ with rGO/PANI = 0.36 exhibits the largest stabilized current density with the highest electroactivity. Clearly, increment in the surface area and electrical conductivity of $C_{Ni-S_{Pd}}/rGP1$ increases electroactivity.

Fig. 10(b) shows the chronopotentiograms of the electrocatalysts at a current density of 1 mA in NaOH 1 M + NaBH₄ 0.1 M solution. All of $C_{Ni-S_{Pd}}/rGP$ polymeric composite electrocatalysts show lower overpotential than $C_{Ni-S_{Pd}}/PANI$. Lower overpotential causes excellent catalytic behavior. These results indicated that $C_{Ni-S_{Pd}}/rGP1$ with rGO/PANI = 0.36 has larger ECSA and electrical conductivity and can supply more active sites for oxidation of BH₄⁻ ions. According to Fig. 10(b), the sequence of overpotentials is as follow: $C_{Ni-S_{Pd}}/rGP1$ < $C_{Ni-S_{Pd}}/rGO$ < $C_{Ni-S_{Pd}}/rGP2$ < $C_{Ni-S_{Pd}}/rGP3$ < $C_{Ni-S_{Pd}}/PANI$. The $C_{Ni-S_{Pd}}/rGP1$ electrocatalyst displays the minimum overpotential (-0.9 V) so it was expected that provides the highest power outputs in DBFC.

The behavior of synthesized catalysts toward BOR was evaluated with EIS in alkaline solution containing 0.06 M NaBH₄ and at the potential of -0.4 V according to our previous studies [31,32] (Fig. 11). In this potential, BH₄⁻ specious are active for oxidation on the surface of the electrocatalysts. The equivalent circuit for fitting EIS curves was depicted in Fig. 11(a). The R_s, R_{ct} and CPE₁ elements describe the electrolyte resistance, charge transfer resistance and double layer capacitance for the electrode. As it can be seen in Fig. 11(b), R_{ct} values for $C_{Ni-S_{Pd}}/PANI$, $C_{Ni-S_{Pd}}/rGO$, $C_{Ni-S_{Pd}}/rGP1$, $C_{Ni-S_{Pd}}/rGP2$ and $C_{Ni-S_{Pd}}/rGP3$ were obtained 252.61, 29.21, 18.90, 71.57 and 111.87 Ω. cm², respectively. As the results show, $C_{Ni-S_{Pd}}/PANI$ and $C_{Ni-S_{Pd}}/rGP1$ have the largest and the lowest charge transfer resistance for borohydride oxidation, respectively. Because as mentioned before PANI support has the lowest electrical conductivity and active surface area but rGP1 support has the highest electrical conductivity and active surface area among polymeric composite supports. With increasing PANI fraction, the loose structure was formed on the surface of reduced graphene oxide; the electrical conductivity of the composite was decreased and caused to increasing the R_{ct} value.

3.4. Single fuel cell studies

For single fuel cell evaluation, 5 cm² active area of MEA was assembled with the loading of 0.5 mg.cm⁻² of Pt/C as cathodic catalyst and 1.0 mg.cm⁻² of $C_{Ni-S_{Pd}}/rGO$, $C_{Ni-S_{Pd}}/PANI$ and $C_{Ni-S_{Pd}}/rGP1$ as anodic electrocatalysts. Among polymeric composite supports, $C_{Ni-S_{Pd}}$ on rGP1 composite were used in fuel cell investigations because the results of three electrode studies showed that this composite support has the excellent performance so it is expected that this composite support has the highest activity in DBHPFC studies. The I-V and I-P curves were recorded in NaOH 2 M + NaBH₄ 1 M (anolyte) and H₂SO₄ 0.5 M + H₂O₂ 2 M (catholyte) as optimum concentrations according to our previous results [58,59].

Comparison the polarization curves of $C_{Ni-S_{Pd}}/PANI$, $C_{Ni-S_{Pd}}/rGO$ and $C_{Ni-S_{Pd}}/rGP1$ at 60 °C were shown in Fig. 12(a). $C_{Ni-S_{Pd}}/PANI$, $C_{Ni-S_{Pd}}/rGO$ and $C_{Ni-S_{Pd}}/rGP1$ delivered maximum power densities of 120.23 mW.cm⁻², 310.20 mW.cm⁻² and 339.10 mW.cm⁻² under similar conditions, respectively. The fuel cell performance of $C_{Ni-S_{Pd}}/rGP1$ catalyst is higher than that of $C_{Ni-S_{Pd}}/PANI$ and $C_{Ni-S_{Pd}}/rGO$ catalysts highlighting the beneficial role of rGP1 as composite support which is also evident by the higher open circuit potential, higher surface area and higher electrical conductivity of $C_{Ni-S_{Pd}}/rGP1$

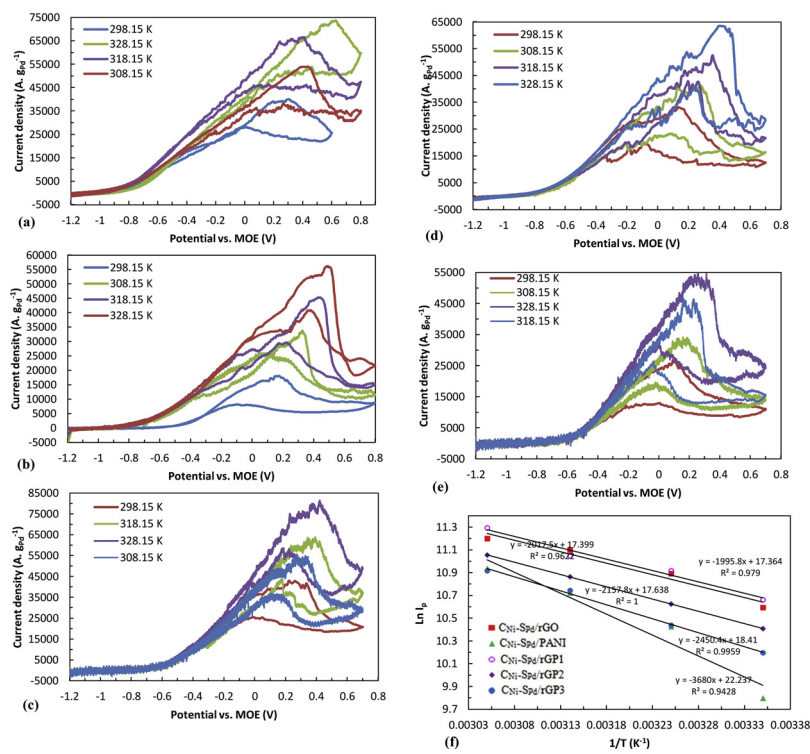


Fig. 9. The effect of temperature on CV curves in NaOH 1 M containing NaBH₄ 0.1 M for (a) C_{Ni}-S_{Pd}/rGO, (b) C_{Ni}-S_{Pd}/PANI, (c) C_{Ni}-S_{Pd}/rGP1, (d) C_{Ni}-S_{Pd}/rGP2 and (e) C_{Ni}-S_{Pd}/rGP3; (f) The plot of I_p vs. 1/T on C_{Ni}-S_{Pd}/rGO, C_{Ni}-S_{Pd}/PANI, C_{Ni}-S_{Pd}/rGP1, C_{Ni}-S_{Pd}/rGP2 and C_{Ni}-S_{Pd}/rGP3 electrocatalysts.

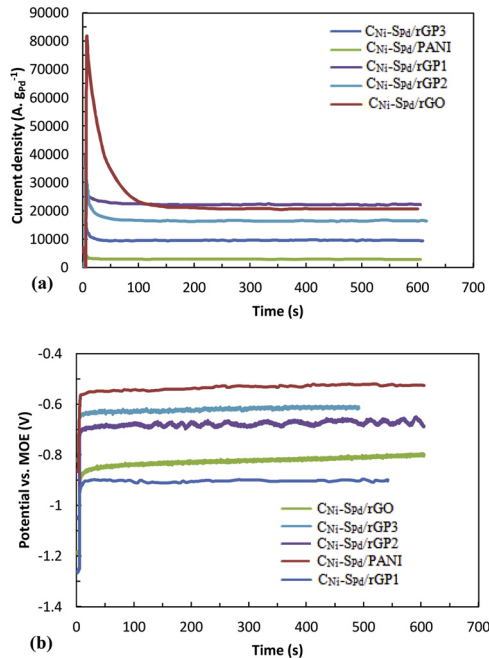


Fig. 10. (a) CA and (b) CP curves for C_{Ni}-S_{Pd}/PANI, C_{Ni}-S_{Pd}/rGO, C_{Ni}-S_{Pd}/rGP1, C_{Ni}-S_{Pd}/rGP2 and C_{Ni}-S_{Pd}/rGP3 electrocatalysts in NaOH 1 M containing NaBH₄ 0.1 M.

electrocatalyst compared to C_{Ni}-S_{Pd}/PANI and C_{Ni}-S_{Pd}/rGO electrocatalysts. As well as, C_{Ni}-S_{Pd}/rGP1 exhibits the lowest slope of the polarization curve respect to C_{Ni}-S_{Pd}/PANI and even C_{Ni}-S_{Pd}/rGO. Therefore, C_{Ni}-S_{Pd}/rGP1 can reduce overpotential of BOR and modify the efficiency of DBHPFC.

An operational stability test was carried out in DBHPFC. The discharging current of 50 mA was applied using homemade electric load system to DBHPFC. The stabled cell voltage of ~1300 V, 1866 V and

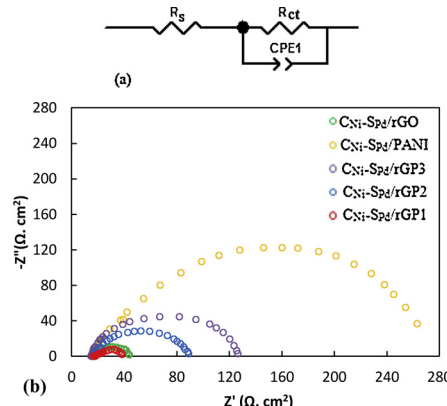


Fig. 11. (a) Equivalent circuit, (b) EIS curves for C_{Ni}-S_{Pd}/PANI, C_{Ni}-S_{Pd}/rGO, C_{Ni}-S_{Pd}/rGP1, C_{Ni}-S_{Pd}/rGP2 and C_{Ni}-S_{Pd}/rGP3 electrocatalysts in NaOH 1 M containing NaBH₄ 0.06 M at -0.4 V.

1910 V was observed over the whole range of operation for C_{Ni}-S_{Pd}/PANI, C_{Ni}-S_{Pd}/rGO and C_{Ni}-S_{Pd}/rGP1, respectively (Fig. 12(b)). As it can be seen in Fig. 12(a), C_{Ni}-S_{Pd}/rGP1 displayed a lower potential fall under the identical exhausting current in agreement with current-voltage and current-power density results. To the best of our knowledge, our data show the highest power density value ever reported compared to previous results based on C_{Ni}-S_{Pd} NPs on different carbon supports or different NPs on polymeric supports presented in Table 2.

The Nyquist plots of EIS in NaBH₄ 1 M + H₂O₂ 2 M for different anodic electrocatalysts (C_{Ni}-S_{Pd}/PANI, C_{Ni}-S_{Pd}/rGO and C_{Ni}-S_{Pd}/rGP1) were presented in Fig. 13(b-d). EIS data were obtained under various temperatures (25 °C and 45 °C) and discharging currents (0 mA and 50 mA) within the frequency range of 100 kHz to 100 mHz. The used equivalent circuit for fitting Nyquist plots was brought in Fig. 13(a) that composed of two time constant equivalent circuit model. R_s is the internal resistance of the Nafion membrane, R_{if} is the interfacial double

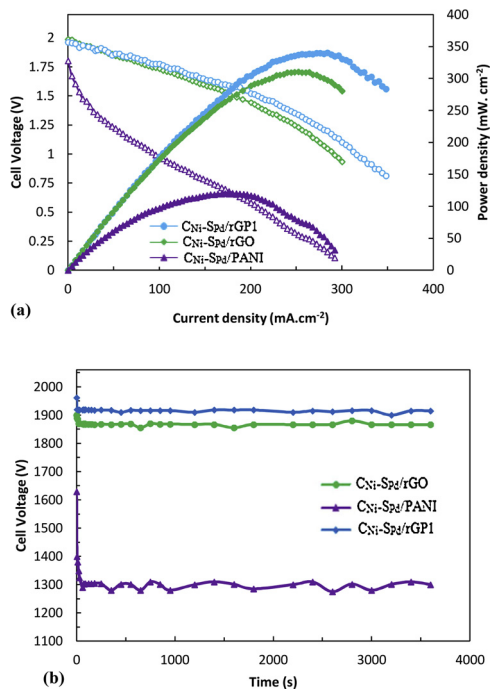


Fig. 12. The influence of $\text{C}_{\text{Ni}}\text{-}\text{Spd}/\text{PANI}$, $\text{C}_{\text{Ni}}\text{-}\text{Spd}/\text{rGO}$ and $\text{C}_{\text{Ni}}\text{-}\text{Spd}/\text{rGP1}$ as anodic electrocatalyst in NaBH_4 1 M, H_2O_2 2 M (a) on current-voltage and current-power density curves at 60 °C, (b) on the stability test data at 50 mA.

layer resistance, CPE_1 is the constant phase element of interfacial double layer, $R_{\text{ct(a+c)}}$ is charge transfer resistance and CPE_2 is the constant phase element of electrodes interface with Nafion. In high frequencies, inductive effects were observed that was result from instrumentation. Other than inductive section, two compressed semicircles were observed. The semicircle which was observed in the high frequencies is related to electrical double layer between membrane-electrodes interface [85]. The later semicircle in the intermediate frequencies is related to charge transfer reaction on the surface of electrodes. The X-intercepts of $\text{C}_{\text{Ni}}\text{-}\text{Spd}/\text{PANI}$, $\text{C}_{\text{Ni}}\text{-}\text{Spd}/\text{rGO}$ and $\text{C}_{\text{Ni}}\text{-}\text{Spd}/\text{rGP1}$ at various temperatures and discharging currents were summarized in Table 3. As the results show, $R_{\text{ct(a+c)}}$ for all anodic electrocatalysts were decreased with increasing temperature from 25 °C to 45 °C and increasing discharging current from 0 to 50 mA because by enhancement of discharging current, $R_{\text{ct(a+c)}}$ reduces according to Eq. (4):

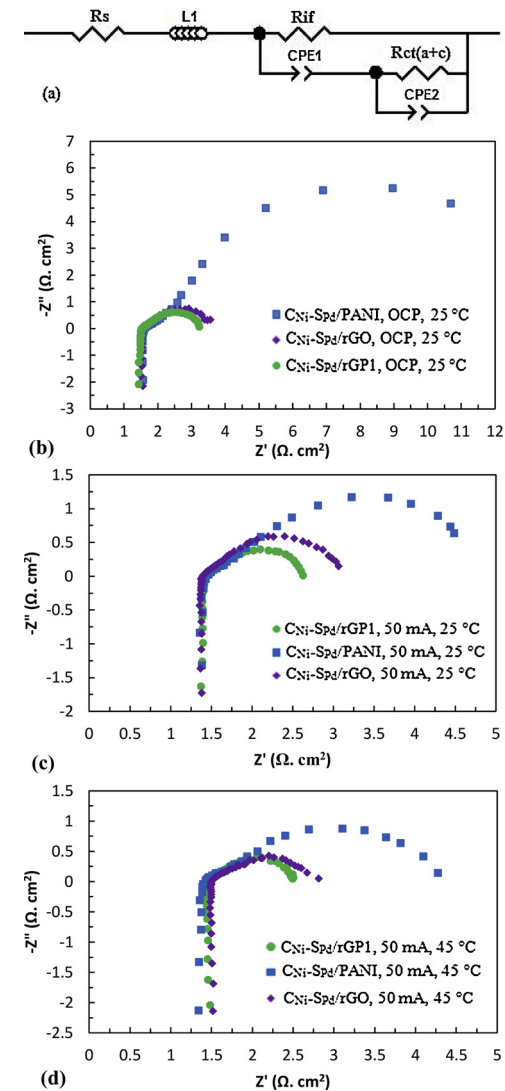


Fig. 13. (a) The equivalent circuit used for fitting EIS spectra in DBPFC, EIS spectra for different anodic electrocatalysts with Pt/C as cathodic catalyst at (b) 25 °C, OCP, (c) 25 °C, 50 mA and (d) 45 °C, 50 mA.

$$R_{\text{ct}} = \frac{dE}{dI} \rightarrow I = \text{constant} (R_{\text{ct}})^{-1} \quad (4)$$

These results showed that the single DBP fuel cell using $\text{C}_{\text{Ni}}\text{-}\text{Spd}/\text{rGP1}$

Table 2
The obtained results about DBFC from literatures at various conditions.

| Anode | Cathode | Anolyte | Catholyt | T (°C) | Power density (mW cm ⁻²) | Ref. |
|--------------------------------------------------------------------------------|-------------------------------------------------------|-------------------------------------------------|----------------------------------------------------------------|--------|--------------------------------------|-----------|
| $\text{C}_{\text{Ni}}\text{-}\text{Spd}/\text{C}$ 1 mg.cm ⁻² | Pt/C 0.5 mg.cm ⁻² | NaOH 2 M + NaBH_4 1 M | H_2O_2 2 M + H_2SO_4 0.5 M | 60 | 200.78 | [32] |
| $\text{C}_{\text{Ni}}\text{-}\text{Spd}/\text{MWCNT}$ 1 mg.cm ⁻² | Pt/C 0.5 mg.cm ⁻² | NaOH 2 M + NaBH_4 1 M | H_2O_2 2 M + H_2SO_4 0.5 M | 60 | 246.82 | [31] |
| $\text{Co(OH)}_2/\text{PPy-C}$ 10 mg.cm ⁻² | $\text{Co(OH)}_2/\text{PPy-C}$ 10 mg.cm ⁻² | NaOH 10 wt% + NaBH_4 5 wt% | O_2 flow rate: 150 mL.min ⁻¹ | 25 | 83 | [83] |
| Pt/PPy 0.5 mg.cm ⁻² | Pt/PPy 0.5 mg.cm ⁻² | NaOH 6 M + NaBH_4 0.3M | H_2O_2 0.1 M + H_2SO_4 0.5M | 25 | 139 | [84] |
| Pt/PPy-C _{35%} 0.6 mg.cm ⁻² | Pt mesh | NaOH 4 M + NaBH_4 1 M | H_2O_2 5 M + HCl 1.5M | 25 | 83.7 | [10] |
| $\text{C}_{\text{Ni}}\text{-}\text{Spd}/\text{PANI}$ 1 mg.cm ⁻² | Pt/C 0.5 mg.cm ⁻² | NaOH 2 M + NaBH_4 1 M | H_2O_2 2 M + H_2SO_4 0.5 M | 60 | 120.23 | This work |
| $\text{C}_{\text{Ni}}\text{-}\text{Spd}/\text{rGO}$ 1 mg.cm ⁻² | Pt/C 0.5 mg.cm ⁻² | NaOH 2 M + NaBH_4 1 M | H_2O_2 2 M + H_2SO_4 0.5 M | 60 | 310.20 | This work |
| $\text{C}_{\text{Ni}}\text{-}\text{Spd}/\text{rGP1}$ 1 mg.cm ⁻² | Pt/C 0.5 mg.cm ⁻² | NaOH 2 M + NaBH_4 1 M | H_2O_2 2 M + H_2SO_4 0.5 M | 60 | 339.10 | This work |

Table 3

The obtained $R_{ct(a+c)}$ values from EIS spectra in DBHPFC for different anodic electrocatalysts with Pt/C as cathodic catalyst at various discharging currents (0 and 50 mA) and temperatures (25 and 45 °C).

| Anodic electrocatalysts | T (°C) | Discharging current (mA) | $R_{ct(a+c)}$ |
|-------------------------|--------|--------------------------|---------------|
| $C_{Ni-S_{Pd}}/PANI$ | 25 | 0 | 12.79 |
| | | 50 | 2.91 |
| $C_{Ni-S_{Pd}}/rGO$ | 45 | 50 | 2.65 |
| | 25 | 0 | 2.20 |
| $C_{Ni-S_{Pd}}/rGP1$ | 45 | 50 | 1.82 |
| | 25 | 0 | 1.36 |
| $C_{Ni-S_{Pd}}/rGP1$ | 45 | 50 | 1.07 |
| | 45 | 50 | 0.93 |

rGP1 as anodic electrocatalyst had the lowest charge transfer resistance, which is identical to the length of the arc.

4. Conclusion

In this present work, $C_{Ni-S_{Pd}}$ NPs with core-shell structure were prepared on rGO, PANI and rGO-PANI polymeric composites with different ratio of rGO to PANI as catalyst supports ($C_{Ni-S_{Pd}}/rGO$, $C_{Ni-S_{Pd}}/PANI$, $C_{Ni-S_{Pd}}/rGP1$, $C_{Ni-S_{Pd}}/rGP2$ and $C_{Ni-S_{Pd}}/rGP3$). The synthesized catalysts were investigated via FE-SEM, EDX, FT-IR, TEM, HR-TEM, XPS and ICP-MS techniques. The electroactivity of the catalysts toward BOR was studied with CV, CA, CP, EIS methods. The consequences of CV curves confirmed that $C_{Ni-S_{Pd}}/rGP1$ has superior electroactivity for BOR. Current density of BOR on $C_{Ni-S_{Pd}}/rGP1$ (42678 A. g⁻¹) is 4.49, 1.71, 1.32 and 1.09 times higher than $C_{Ni-S_{Pd}}/PANI$ (17072 A. g⁻¹), $C_{Ni-S_{Pd}}/rGP3$ (24954 A. g⁻¹), $C_{Ni-S_{Pd}}/rGP2$ (32260 A. g⁻¹) and $C_{Ni-S_{Pd}}/rGO$ (39085 A. g⁻¹), respectively. The effect of temperature on CV curves was investigated and E_a were calculated using Arrhenius equation. As expected, among the synthesized electrocatalysts, $C_{Ni-S_{Pd}}/rGP1$ has the lowest activation energy (16.59 kJ.mol⁻¹) and so shows the highest catalytic activity for BOR. The results of CA and CP curves showed that among the synthesized electrocatalysts, $C_{Ni-S_{Pd}}/rGP1$ has the highest steady state current density and the lowest overpotential for BOR. Also, the results of EIS spectra verified the results of CV, CA and CP because $C_{Ni-S_{Pd}}/rGP1$ indicated the lowest charge transfer resistance (18.90 Ω. cm²) respect to other electrocatalysts.

As well as, the performance of $C_{Ni-S_{Pd}}/PANI$, $C_{Ni-S_{Pd}}/rGO$ and $C_{Ni-S_{Pd}}/rGP1$ as anodic electrocatalysts on the performance of DBHPFC was evaluated and $C_{Ni-S_{Pd}}/rGP1$ was selected as suitable anodic electrocatalyst with maximum power density of 339.10 mWcm⁻². On the other hands, $C_{Ni-S_{Pd}}/rGP1$ was improved power generation equal with 64.54% and 8.52% respect to $C_{Ni-S_{Pd}}/PANI$ (120.23 mW.cm⁻²) and $C_{Ni-S_{Pd}}/rGO$ (310.20 mW.cm⁻²), respectively. In addition, the results of cell impedance indicated that $C_{Ni-S_{Pd}}/rGP1$ has the lowest $R_{ct(a+c)}$ at different discharging currents and temperatures respect to $C_{Ni-S_{Pd}}/rGO$ and $C_{Ni-S_{Pd}}/PANI$ electrocatalysts.

Acknowledgements

This study was supported by Nanotechnology Initiative Council, University of Tabriz and Near East University in North Cyprus. The authors would like to thank O. Mermec and A. Farzaneh for assistance in the measurement of XPS spectra.

Appendix A. Supplementary data

Supplementary material related to this article can be found, in the online version, at doi:<https://doi.org/10.1016/j.apcatb.2019.03.064>.

References

- [1] S. Dai, Z. Liu, B. Zhao, J. Zeng, H. Hu, Q. Zhang, D. ChangChen, C. Qu, D. Dang, M. Liu, A high-performance supercapacitor electrode based on N-doped porous graphene, *J. Power Sources* 387 (2018) 43–48.
- [2] M.A. Deyab, Ionic liquid as an electrolyte additive for high performance lead-acid batteries, *J. Power Sources* 390 (2018) 176–180.
- [3] C. Wang, Y. Li, C. Zhang, L. Shi, S. Tong, B. Guo, J. Zhang, J. He, Y. Gaoa, C. Su, J. Yang, Enhancing the performance of planar heterojunction perovskite solar cells using stable semiquinone and amine radical modified hole transport layer, *J. Power Sources* 390 (2018) 134–141.
- [4] S. Zhang, Y. Zhang, J. Chen, C. Yin, X. Liu, Design, fabrication and performance evaluation of an integrated reformed methanol fuel cell for portable use, *J. Power Sources* 389 (2018) 37–49.
- [5] A.M. Herring, T.A.J. Zawodzinski, S.J. Hamrock, Status of fuel cells and the challenges facing fuel cell technology today, *Fuel Cell Chemistry and Operation; ACS Symposium Series*, American Chemical Society, Washington, DC, 2010.
- [6] P. Kanninen, M. Borghei, O. Sorsa, E. Pohjalainen, E.I. Kauppinen, V. Ruiz, T. Kallio, Highly efficient cathode catalyst layer based on nitrogen-doped carbon nanotubes for the alkaline direct methanol fuel cell, *Appl. Catal. B Environ.* (2014) 156–157 341–349.
- [7] M.S. Saha, R. Li, X. Sun, S. Ye, 3-D composite electrodes for high performance PEM fuel cells composed of Pt supported on nitrogen-doped carbon nanotubes grown on carbon paper, *Electrochim. Commun.* 11 (2) (2009) 438–441.
- [8] M. Chatenet, F. Micoud, I. Roche, E. Chainet, Kinetics of sodium borohydride direct oxidation and oxygen reduction in sodium hydroxide electrolyte - Part I. BH_4^- electro-oxidation on Au and Ag catalysts, *Electrochim. Acta* 51 (2006) 5459–5467.
- [9] B.H. Liu, Z.P. Li, S. Suda, Electrocatalysts for the anodic oxidation of borohydrides, *Electrochim. Acta* 49 (2004) 3097–3105.
- [10] R.C.P. Oliveira, J. Milikic, E. Das, A.B. Yurtcan, D.M.F. Santos, B. Sljukic, Platinum/polypyrrole-carbon electrocatalysts for direct borohydride-peroxide fuel cells, *Appl. Catal. B: Environ.* 238 (2018) 454–464.
- [11] C. Grimmer, M. Grandi, R. Zacharias, B. Cermeneck, H. Weber, C. Morais, T.W. Napporn, S. Weinberger, A. Schenk, V. Hacker, The electrooxidation of borohydride: a mechanistic study on palladium (Pd/C) applying RRDE, 11B-NMR and FTIR, *Appl. Catal. B Environ.* 180 (2016) 614–621.
- [12] I. Merino-Jimenez, M.J. Janik, C.Pd. Leon, F.C. Walsh, Pd-Ir alloy as an anode material for borohydride oxidation, *J. Power Sources* 269 (2014) 498–508.
- [13] J. Liu, L. Yi, X. Wang, Q. Zhao, Y. Zhang, J. Gao, W. Wei, Investigation of nanoporous carbon supported palladium-zinc nanocomposites as anode catalysts for direct borohydride/hydrogen peroxide fuel cell, *Int. J. Hydrogen Energy* 40 (2015) 7301–7307.
- [14] J. Liu, Q. Zhao, S. Chen, L. Yi, X. Wang, W. Wei, Nanoporous carbon supported platinum-copper nanocomposites as anode catalysts for direct borohydride-hydrogen peroxide fuel cell, *Electrochim. Acta* 171 (2015) 96–104.
- [15] J. Ma, Y. Sahai, R.G. Buchheit, Direct borohydride fuel cell using Ni-based composite anodes, *J. Power Sources* 195 (2010) 4709–4713.
- [16] F. Pei, Y. Wang, X. Wang, P. He, Q. Chen, X. Wang, Performance of supported Au-Co alloy as the anode catalyst of direct borohydride-hydrogen peroxide fuel cell, *Int. J. Hydrogen Energy* 35 (2010) 8136–8142.
- [17] B. Sljukic, J. Milikic, D.M.F. Santos, C.A.C. Sequeir, Carbon-supported $Pt_{0.75}M_{0.25}$ ($M = Ni$ or Co) electrocatalysts for borohydride oxidation, *Electrochim. Acta* 107 (2013) 577–583.
- [18] L. Tamasauskait-Tamasuniuit, A. Radomskis, K. Antanaviciut, J. Jablonskien, A. Balcuniuit, A. Zieli, L. Naruskevicius, R. Kondrotas, E. Norkus, Graphene supported platinum-cobalt nanocomposites as electrocatalysts for borohydride oxidation, *Int. J. Hydrogen Energy* 39 (2014) 4282–4290.
- [19] G.J. Wang, Y.Z. Gao, Z.B. Wang, C.Y. Du, J.J. Wang, G.P. Yin, Investigation of PtNi/C anode electrocatalysts for direct borohydride fuel cell, *J. Power Sources* 195 (2010) 185–189.
- [20] L. Yi, L. Liu, X. Liu, X. Wang, W. Yi, P. He, et al., Carbon supported Pt-Co nanoparticles as anode catalyst for borohydride-hydrogen peroxide fuel cell: electrocatalysis and fuel cell performance, *Int. J. Hydrogen Energy* 37 (2012) 12650–12658.
- [21] R. Huang, Y.H. Wen, G.F. Shao, S.G. Sun, Insight into the melting behavior of Au–Pt core–Shell nanoparticles from atomistic simulations, *J. Phys. Chem. C* 117 (2013) 4278–4286.
- [22] M. Tsuji, R. Matsuo, P. Jiang, N. Miyamae, D. Ueyama, M. Nishio, S. Hikino, H. Kumagae, K.S.N. Kamarudin, X.L. Tang, Shape-dependent evolution of Au@Ag core–Shell nanocrystals by PVP-Assisted N,N-Dimethylformamide reduction, *Cryst. Growth Des.* 8 (2008) 2528–2536.
- [23] D. Duan, J. Liang, H. Liu, X. You, H. Wei, G. Wei, S. Liu, The effective carbon supported core-shell structure of Ni@Au catalysts for electro-oxidation of borohydride, *Int. J. Hydrogen Energy* 40 (2015) 488–500.
- [24] D. Duan, X. You, J. Liang, S. Liu, Y. Wang, Carbon supported Cu-Pd nanoparticles as anode catalyst for direct borohydride-hydrogen peroxide fuel cells, *Electrochim. Acta* 176 (2015) 1126–1135.
- [25] D. Duan, H. Liu, X. You, H. Wei, S. Liu, Anodic behavior of carbon supported Cu@Ag core-shell nanocatalysts in direct borohydride fuel cells, *J. Power Sources* 293 (2015) 292–300.
- [26] D. Duan, Q. Wang, H. Liu, X. You, S. Liu, Y. Wang, Investigation of carbon-supported Ni@Ag core-shell nanoparticles as electrocatalyst for electrooxidation of sodium borohydride, *J. Solid State Electrochem.* 20 (2016) 2699–2711.
- [27] H. Wang, Y. Wang, X. Wang, P. He, L. Yi, W. Yi, X. Liu, Investigation of the performance of $Au_{core-Pd_{shell}}/C$ as the anode catalyst of direct borohydride-hydrogen peroxide fuel cell, *Int. J. Electrochim. Sci.* (2011) 1–6.
- [28] R.L. Arevalo, M.C.S. Escano, E. Gyenge, H. Kasai, A theoretical study of the structure and stability of borohydride on 3d transition metals, *Surf. Sci.* 606 (2012) 1954–1959.
- [29] P. Panagiotopoulou, D.I. Kondarides, Effect of the nature of the support on the

catalytic performance of noble metal catalysts for the water-gas shift reaction, *Catal. Today* 112 (2006) 49–52.

[30] V.R. Stamenkovic, B. Fowler, B.S. Mun, G. Wang, P.N. Ross, C.A. Lucas, e. al, Improved oxygen reduction activity on Pt₃Ni(111) via increased surface site availability, *Science* 315 (2007) 493–497.

[31] M.G. Hosseini, R. Mahmoodi, Improvement of energy conversion efficiency and power generation in direct borohydride-hydrogen peroxide fuel cell: the effect of Ni-M core-shell nanoparticles (M = Pt, Pd, Ru)/Multiwalled Carbon Nanotubes on the cell performance, *J. Power Sources* 370 (2017) 87–97.

[32] M.G. Hosseini, R. Mahmoodi, Ni@M. (M = Pt, Pd and Ru) core@shell nanoparticles on Vulcan XC-72R support with superior catalytic activity toward borohydride oxidation: electrochemical and fuel cell studies, *New J. Chem.* 41 (2017) 13408–13417.

[33] B. Fang, J.H. Kim, M. Kim, J.-S. Yu, Ordered hierarchical nanostructured carbon as a highly efficient cathode catalyst support in proton exchange membrane fuel cell, *Chem. Mater.* 21 (2009) 789–796.

[34] J.L. Reyes-Rodríguez, F. Godínez-Salomon, M.A. Leyva, O. Solorza-Feria, RRDE study on Co@Pt/C core-shell nanocatalysts for the oxygen reduction reaction, *Int. J. Hydrogen Energy* 38 (2013) 12634–12639.

[35] D. Duan, S. Liu, C. Yang, Z. Zhang, X. Hao, G. Wei, Y. Li, Electrocatalytic performance of Ni_{core}@Pt_{shell}/C core-shell nanoparticle with the Pt in nanoshell, *Int. J. Hydrogen Energy* 38 (2013) 14261–14268.

[36] S. Ali, R. Ahmed, M. Sohail, S.A. Khan, M.S. Ansari, Co@Pt core-shell nanoparticles supported on carbon nanotubes as promising catalyst for methanol electro-oxidation, *J. Ind. Eng. Chem.* 28 (2015) 344–350.

[37] N. Muthuswamy, J.L.G.D. Fuente, D.T. Tran, J. Walmsley, M. Tsyplkin, S. Raaen, S. Sunde, M. Rønning, D. Chen, Ru@Pt core-shell nanoparticles for methanol fuel cell catalyst: control and effects of shell composition, *Int. J. Hydrogen Energy* 38 (2013) 16631–16641.

[38] K.S. Novoselov, A.K. Geim, S.V. Morozov, D. Jiang, Y. Zhang, S.V. Dubonos, I.V. Grigorieva, A.A. Firsov, Electric field effect in atomically thin carbon films, *Science* 306 (2004) 666–669.

[39] A.A. Balandin, S. Ghosh, W.Z. Bao, I. Calizo, D. Teweldebrhan, F. Miao, C.N. Lau, Superior thermal conductivity of single-layer graphene, *Nano Lett.* 8 (2008) 902–907.

[40] C. Lee, X.D. Wei, J.W. Kysar, J. Hone, Measurement of the elastic properties and intrinsic strength of monolayer graphene, *Science* 321 (2008) 385–388.

[41] S. Park, R.S. Ruoff, Chemical methods for the production of graphenes, *Nat. Nanotechnol.* 4 (2009) 217–224.

[42] M.H. Liang, L.J. Zhi, Graphene-based electrode materials for rechargeable Lithium batteries, *J. Mater. Chem.* 19 (2009) 5871–5878.

[43] S. Stankovich, D.A. Dikin, G.H.B. Dommett, K.M. Kohlhaas, E.J. Zimney, E.A. Stach, R.D. Piner, S.T. Nguyen, R.S. Ruoff, Graphene-based composite materials, *Nature* 442 (2006) 282–286.

[44] W. Yang, K.R. Ratinac, S.P. Ringer, P. Thordarson, J.J. Gooding, F. Braet, Carbon nanomaterials in biosensors: should you use nanotubes or graphene? *Angew. Chem. Int. Ed.* 49 (2010) 2114–2138.

[45] S.-S. Li, J.-J. Lv, L.-N. Teng, A.-J. Wang, J.-R. Chen, J.-J. Feng, Facile synthesis of PdPt@Pt nanorings supported on reduced graphene oxide with enhanced electrocatalytic properties, *ACS Appl. Mater. Interfaces* 6 (13) (2014) 10549–10555.

[46] X. Zhong, H. Yu, X. Wang, L. Liu, Y. Jiang, L. Wang, G. Zhuang, Y. Chu, X. Li, J.-G. Wang, Pt@Au nanorods uniformly decorated on pyridine cycloaddition graphene as a highly effective electrocatalyst for oxygen reduction, *ACS Appl. Mater. Interfaces* 6 (2014) 13448–13454.

[47] J.-N. Zheng, S.-S. Li, X. Ma, F.-Y. Chen, A.-J. Wang, J.-R. Chen, J.-J. Feng, Green synthesis of core-shell gold-palladium@palladium nanocrystals dispersed on graphene with enhanced catalytic activity toward oxygen reduction and methanol oxidation in alkaline media, *J. Power Sources* 262 (2014) 270–278.

[48] M. Zhang, Y. Li, Z. Yan, J. Jing, J. Xie, M. Chen, Improved catalytic activity of cobalt core–platinum shell nanoparticles supported on surface functionalized graphene for methanol electro-oxidation, *Electrochim. Acta* 158 (2015) 81–88.

[49] D. Chen, Y. Zhao, Y. Fan, W. Wang, X. Li, X. Peng, X. Wang, J. Tian, Preparation and characterization of core-shell-like PbPt nanoparticles electro-catalyst supported on graphene for methanol oxidation, *Int. J. Hydrogen Energy* 39 (2014) 116053–116060.

[50] M. Fang, K.G. Wang, H.B. Lu, Y.L. Yang, S. Nutt, Covalent polymer functionalization of graphene nanosheets and mechanical properties of composites, *J. Mater. Chem. Phys.* 19 (2009) 7098–7105.

[51] C. Li, H. Bai, G.Q. Shi, Conducting polymer nanomaterials: electrosynthesis and applications, *Chem. Soc. Rev.* 38 (2009) 2397–2409.

[52] D. Li, J.X. Huang, R.B. Kaner, Polyaniline nanofibers: a unique polymer nanosstructure for versatile applications, *Acc. Chem. Res.* 42 (2009) 135–145.

[53] Y.K. Zhou, B.L. He, W.J. Zhou, J.E. Huang, X.H. Li, B. Wu, H.L. Li, Electrochemical capacitance of well-coated single-walled carbon nanotube with polyaniline composites, *Electrochim. Acta* 49 (2004) 257–262.

[54] S.M. Golabi, A. Nozad, Electrocatalytic oxidation of methanol at lower potentials on glassy carbon electrode modified by platinum and platinum alloys incorporated in poly(o-Aminophenol) film, *Electroanalysis* 15 (2003) 278–286.

[55] I. Bicerik, S. Suser, F. Kadırgan, Electrooxidation of methanol on doped polypyrrole films in acidic media, *J. Electroanal. Chem.* 502 (2001) 118–125.

[56] W.S. Hummers, R.E. Offeman, Preparation of Graphitic Oxide, (1958), p. 1339.

[57] H. Tang, S. Wang, M. Pan, S.P. Jiang, Y. Ruan, Performance of direct methanol fuel cells prepared by hot-pressed MEA and catalyst-coated membrane (CCM), *Electrochim. Acta* 52 (2007) 3714–3718.

[58] M.G. Hosseini, R. Mahmoodi, The comparison of direct borohydride-hydrogen peroxide fuel cell performance with membrane electrode assembly prepared by catalyst coated membrane method and catalyst coated gas diffusion layer method using Ni@Pt/C as anodic catalyst, *Int. J. Hydrogen Energy* 42 (2017) 10363–10375.

[59] M.G. Hosseini, R. Mahmoodi, Preparation method of Ni@Pt/C nanocatalyst affects the performance of direct borohydride-hydrogen peroxide fuel cell: improved power density and increased catalytic oxidation of borohydride, *J. Colloid Interface Sci.* 500 (2017) 264–275.

[60] S. Saha, S. Ganguly, D. Banerjee, K. Kargupta, Novel bimetallic graphene-cobalt-nickel (G-Co-Ni) nano-ensemble electrocatalyst for enhanced borohydride oxidation, *Int. J. Hydrogen Energy* 40 (2015) 1760–1773.

[61] Y. Zhao, X. Yang, J. Tian, F. Wang, L. Zhan, Methanol electro-oxidation on Ni@Pd core-shell nanoparticles supported on multi-walled carbon nanotubes in alkaline media, *Int. J. Hydrogen Energy* 35 (2010) 3249–3257.

[62] Y. Chen, F. Yang, Y. Dai, W. Wang, S. Chen, Ni@Pt core-shell nanoparticles: synthesis, structural and electrochemical properties, *J. Phys. Chem. C* 112 (2008) 1645–1649.

[63] R. Ojani, R. Valiollahi, J.B. Raoof, Au hollow nanospheres on graphene support as catalyst for sodiumborohydride electrooxidation, *Appl. Surf. Sci.* 311 (2014) 245–251.

[64] H. Xu, J. Zhang, Y. Chen, H. Lu, J. Zhuang, Electrochemical polymerization of polyaniline doped with Cu²⁺ as the electrode material for electrochemical supercapacitors, *RSC Adv.* 4 (2014) 5547–5552.

[65] B. Marjanovic, I. Juranic, S. Mentus, G. Ceric-Marjanovic, P. Holler, Oxidative polymerization of anilinium 5-sulfosalicylate with peroxydisulfate in water, *Chem. Papers* 64 (6) (2010) 783–790.

[66] J.N. Gavagni, A.H. Hasani, M. Nouri, M. Mahyari, A.R. Salehi, Highly sensitive and flexible ammonia sensor based on S and N co-doped graphene quantum dots/polyaniline hybrid at room temperature, *Sens. Actuators B* 229 (2016) 239–248.

[67] Z. Wu, X. Chen, S. Zhu, Z. Zhou, Y. Yao, W. Quan, B. Liu, Enhanced sensitivity of ammonia sensor using graphene/polyaniline nanocomposite, *Sens. Actuators B* 178 (2013) 485–493.

[68] Z. Wu, X. Chen, S. Zhu, Z. Zhou, Y. Yao, W. Quan, B. Liu, Room temperature methane sensor based on graphene nanosheets/polyaniline nanocomposite thin film, *IEEE Sens. J.* 13 (2013) 777–782.

[69] A. Ganguly, S. Sharma, P. Papakonstantinou, J. Hamilton, Probing the thermal deoxygenation of graphene oxide using high-resolution in situ X-ray-Based spectroscopies, *J. Phys. Chem. C* 115 (2011) 17009–17019.

[70] K. Sharma, K. Maiti, N.H. Kim, D. Hui, J.H. Lee, Green synthesis of glucose-reduced graphene oxide supported Ag-Cu₂O nanocomposites for the enhanced visible-light photocatalytic activity, *Composites Part B* 138 (2018) 35–44.

[71] M.G. Hosseini, N. Rashidi, R. Mahmoodi, M. Omer, Preparation of Pt/G and PtNi/G nanocatalysts with high electrocatalytic activity for borohydride oxidation and investigation of different operation condition on the performance of direct borohydride-hydrogen peroxide fuel cell, *Mater. Chem. Phys.* 208 (2018) 207–219.

[72] B.J. Kim, S.G. Oh, M.G. Han, S.S. Im, Preparation of polyaniline nanoparticles in micellar solutions as polymerization medium, *Langmuir* 16 (2000) 5841–5845.

[73] Y. Yang, Y. Xi, J. Li, G. Wei, N.I. Klyui, W. Han, Flexible supercapacitors based on polyaniline arrays coated graphene aerogel electrodes, *nanoscale res. Lett.* 12 (2017) 394–403.

[74] S. Eris, Z. Dasdelen, Y. Yıldız, F. Sen, Nanostructured Polyaniline-rGO decorated platinum catalyst with enhanced activity and durability for Methanol oxidation, *Int. J. Hydrogen Energy* 43 (2018) 1337–1343.

[75] M. Kim, C. Lee, J. Jang, Fabrication of highly flexible, scalable, and high-performance supercapacitors using Polyaniline/Reduced graphene oxide film with enhanced electrical conductivity and crystallinity, *Adv. Funct. Mater.* 24 (17) (2014) 2489–2499.

[76] X. Huang, N. Hu, R. Gao, Y. Yu, Y. Wang, Z. Yang, E.S. Kong, H. Wei, Y. Zhang, Reduced graphene oxide-polyaniline hybrid: preparation, characterization and its applications for ammonia gas sensing, *J. Mater. Chem.* 22 (2012) 22488–22495.

[77] R. Wang, L. Huang, X. Tian, Understanding the protonation of polyaniline and polyaniline-graphene interaction, *J. Phys. Chem. C* 116 (2012) 13120–13126.

[78] L. Ding, Z. Qin, Z. Dou, Y. Shen, Y. Cai, Y. Zhang, Y. Zhou, Morphology-promoted synergistic effects on the sensing properties of polyaniline ultrathin layers on reduced graphene oxide sheets for ammonia and formaldehyde detection, *J. Mater. Sci.* 53 (2018) 7595–7608.

[79] Y. Sun, S.R. Wilson, D.I. Schuster, High dissolution and strong light emission of carbon nanotubes in aromatic amine solvents, *J. Am. Chem. Soc.* 123 (2001) 5348–5349.

[80] X.Y. Ting, L.S. Juan, P.X. Liang, L.W. -Ang, G. Jean-Yves, D.L. Zong, In situ chemical fabrication of polyaniline/multi-walled carbon nanotubes composites as supports of Pt for methanol electrooxidation, *Sci. China Chem.* 53 (9) (2010) 2006–2014.

[81] A. De, J. Datta, I. Haldar, M. Biswas, Catalytic intervention of MoO₃ toward ethanol oxidation on PtPd nanoparticles decorated MoO₃-polypyrrole composite support, *ACS Appl. Mater. Interfaces* 8 (42) (2016) 28574–28584.

[82] M.G. Hosseini, M.M. Momeni, M. Faraji, Highly active nickel nanoparticles supported on TiO₂ nanotube electrodes for methanol electrooxidation, *Electroanalysis* 22 (2010) 2620–2625.

[83] H.Y. Qin, Z.X. Liu, L.Q. Ye, J.K. Zhu, Z.P. Li, The use of polypyrrole modified carbon-supported cobalt hydroxide as cathode and anode catalysts for the direct borohydride fuel cell, *J. Power Sources* 192 (2009) 385–390.

[84] K. Sombatmankhong, Improved performance and stability of direct borohydride fuel cells (DBFCs) with porous polypyrrole support, *J. Porous Mater.* 22 (2015) 675–687.

[85] C.M. Lai, J.C. Lin, K.L. Hsueh, C.P. Hwang, K.C. Tsay, L.D. Tsai, On the electrochemical impedance spectroscopy of direct methanol fuel cell, *Int. J. Hydrogen Energy* 32 (2007) 4381–4388.